Title

Modelling reverberation mapping data – II. Dynamical modelling of the Lick AGN Monitoring Project 2008 data set

Permalink

Journal

ISSN

Authors

Pancoast, Anna
Brewer, Brendon J
Treu, Tommaso
et al.

Publication Date

DOI

Peer reviewed

Modeling reverberation mapping data II: dynamical modeling of the Lick AGN Monitoring Project 2008 dataset

Anna Pancoast[1], Brendon J. Brewer[2], Tommaso Treu[1,6], Daeseong Park[3,4],
Aaron J. Barth[4], Misty C. Bentz[5], and Jong-Hak Woo[3]

[1] *Department of Physics, University of California, Santa Barbara, CA 93106, USA; pancoast@physics.ucsb.edu*
[2] *Department of Statistics, The University of Auckland, Private Bag 92019, Auckland 1142, New Zealand*
[3] *Astronomy Program, Department of Physics and Astronomy, Seoul National University, Seoul 151-742, Republic of Korea*
[4] *Department of Physics & Astronomy, 4129 Frederick Reines Hall, University of California, Irvine, CA 92697-4575, USA*
[5] *Department of Physics and Astronomy, Georgia State University, Atlanta, GA 30303, USA*
[6] *Current address: Physics and Astronomy Building, 430 Portola Plaza, Box 951547, Los Angeles, CA 90095-1547, USA*

19 January 2015

ABSTRACT

We present dynamical modeling of the broad line region (BLR) for a sample of five Seyfert 1 galaxies using reverberation mapping data taken by the Lick AGN Monitoring Project in 2008. By modeling the AGN continuum light curve and Hβ line profiles directly we are able to constrain the geometry and kinematics of the BLR and make a measurement of the black hole mass that does not depend upon the virial factor, f, needed in traditional reverberation mapping analysis. We find that the geometry of the BLR is generally a thick disk viewed close to face-on. While the Hβ emission is found to come preferentially from the far side of the BLR, the mean size of the BLR is consistent with the lags measured with cross-correlation analysis. The BLR kinematics are found to be consistent with either inflowing motions or elliptical orbits, often with some combination of the two. We measure black hole masses of $\log_{10}(M_{\rm BH}/M_\odot) = 6.62^{+0.10}_{-0.13}$ for Arp 151, $7.42^{+0.26}_{-0.27}$ for Mrk 1310, $7.51^{+0.23}_{-0.14}$ for NGC 5548, $6.42^{+0.24}_{-0.18}$ for NGC 6814, and $6.99^{+0.32}_{-0.25}$ for SBS 1116+583A. The f factors measured individually for each AGN are found to correlate with inclination angle, although not with $M_{\rm BH}$, L_{5100}, or FWHM/σ of the emission line profile.

Key words: galaxies: active – galaxies: nuclei – methods: statistical

1 INTRODUCTION

While active galactic nuclei (AGNs) are thought to be powered by accretion onto supermassive black holes at the centers of most galaxies, the geometry and dynamics of the surrounding regions are not well understood. In the standard model of AGNs (Antonucci 1993; Urry & Padovani 1995), the region directly outside the accretion disk is the broad line region (BLR), where broad line emitting gas moves at velocities of 10^{3-4} km s^{-1} within the Keplerian potential of the black hole. Measurements of the distance of this gas from the central ionizing source in the accretion disk are on the order of light days for lower luminosity AGNs such as Seyfert galaxies and this distance increases with AGN luminosity (Wandel et al. 1999; Kaspi et al. 2000; Bentz et al. 2006, 2013).

The geometry and dynamics of the BLR can be further constrained by reverberation mapping measurements,

where changes in the AGN continuum emission are monitored alongside the echo of these same changes in the BLR emission lines (Blandford & McKee 1982; Peterson 1993; Peterson et al. 2004). The time lag τ between changes in the AGN continuum flux and those of the broad emission lines is interpreted as a measure of the average radius of the BLR and traditionally measured using the cross-correlation function. The time lag can then be combined with BLR gas velocities v taken from the width of the broad emission line to measure a virial product that has the dimensions of black hole mass. The virial product $M_{\rm vir} = c\tau v^2/G$ is related to the true black hole mass $M_{\rm BH}$ by a dimensionless virial factor f of order unity that is calibrated by aligning the $M_{\rm BH} - \sigma_*$ relations for active and inactive galaxies (Onken et al. 2004; Collin et al. 2006; Woo et al. 2010; Greene et al. 2010b; Graham et al. 2011; Park et al. 2012b; Woo et al. 2013; Grier et al. 2013b). Currently, the uncertainty in mean f of ~ 0.4 dex is the largest uncertainty in reverber-

ation mapped black hole masses (e.g. Park et al. 2012b). Since the sample of ~ 50 reverberation mapped AGNs is responsible for calibrating single-epoch M_{BH} estimates applied to much larger samples of AGNs through the BLR-size-to-luminosity relation (Vestergaard & Peterson 2006; McGill et al. 2008; Vestergaard 2011), it is important to measure M_{BH} in reverberation mapped AGNs with as few assumptions and added uncertainties as possible.

There is more information in high quality reverberation mapping data than a single estimate of the time lag. This is illustrated by analysis of high-quality datasets that show clear velocity-resolved lag structure across the emission line profile in a number of AGNs. Many of these velocity-resolved lag estimates are consistent with bound orbits in a Keplerian potential (Bentz et al. 2009; Denney et al. 2010; Barth et al. 2011a,b; Grier et al. 2013a), but some show additional kinematic signatures consistent with inflowing or outflowing gas (Bentz et al. 2009; Denney et al. 2010; Grier et al. 2013a), where non-gravitational forces may be at work. Much recent work has focused on trying to recover this additional information about the BLR geometry and dynamics through more sophisticated analysis techniques. One method for doing this is to recover the transfer function, which is the distribution of time lags either for the integrated emission line flux or as a function of line-of-sight velocity (see Bentz et al. 2010; Grier et al. 2013a, and references therein). This is the approach used in the code MEMECHO, which recovers the transfer function using a flexible parameterization for the transfer function shape and prevents over-fitting by asserting that the solution has a high entropy (Horne et al. 1991; Horne 1994). The main advantage to recovering the transfer function is that it does not require adopting any specific model for the geometry and dynamics of the BLR (see Krolik & Done 1995, for an application of a pixelated method to the reconstruction of the transfer function). This also means that in order to relate features in the recovered transfer function to geometrical and dynamical properties of the BLR at a quantitative level, models must eventually be constructed and compared to the transfer function.

Members of our team have been working on an alternative approach that involves modeling reverberation mapping data directly to constrain the geometry and dynamics of the BLR (see Pancoast et al. 2011; Brewer et al. 2011a; Pancoast et al. 2012). While this method requires adopting a specific BLR model, the direct modeling approach is quite general and allows for the use of any BLR model whose consequences are fast to compute. The direct modeling method can then be used to determine which theoretical models of the BLR geometry and dynamics are preferred by the data. By formulating the method as a problem of Bayesian inference, parameter estimation (within the context of a particular BLR model), and model selection (comparison of distinct BLR models) are both possible. In addition to constraining the geometry and dynamics of the broad line emitting gas, the direct modeling approach allows for independent measurement of the black hole mass without relying on the normalizing factor f required by the traditional analysis. This means that with high-quality reverberation mapping datasets, the uncertainty in black hole masses from dynamical modeling could be substantially less than the ~ 0.4 dex introduced by assuming a mean value for f (Pancoast et al. 2011). Finally, independent estimates of the black hole mass

can be compared to M_{vir} to obtain measurements of f for individual AGNs. With a large enough sample of AGNs with individual f values from direct modeling, we have another method of calculating a mean f factor for different AGN populations.

The direct modeling method works by using the continuum flux light curve and a model of the geometry and dynamics of the BLR to create a time series of simulated broad emission line profiles. The simulated line profiles can then be directly compared to the reverberation mapping data line profiles to infer which BLR model parameter values best reproduce the data. Working with the formalism of Bayesian inference, we calculate the joint posterior probability distribution function (PDF) for the model parameters. We have focused on developing a simply parametrized phenomenological model of the BLR to map the density of broad line emission in position and velocity space. We have purposefully excluded any constraints from photoionization physics or radiative transfer at this stage, because doing so requires assuming a relation between the distribution of broad line flux emission and the distribution and density of the emitting gas. While extending the model to infer the physics of the BLR gas is certainly of interest, we have found that a flexible simply parameterized model is sufficient to reproduce the line profile shape and variability characteristics in current reverberation mapping spectral datasets as demonstrated for Arp 151 and Mrk 50 (e.g. Brewer et al. 2011a; Pancoast et al. 2012).

In addition to a model of the BLR, it is necessary to include a model for the AGN continuum light curve, since it is necessary to evaluate the AGN continuum flux at arbitrary times to produce simulated broad emission line profiles. We use Gaussian processes to interpolate between the continuum light curve datapoints, which allows us to include the uncertainty from the interpolation process into the final uncertainty on the BLR model parameters. The simplified version of Gaussian processes that we use is the same as a continuous time first-order autoregressive process (CAR(1)), which has been found to be a good model for larger samples of AGN light curves (Kelly et al. 2009; Kozłowski et al. 2010; MacLeod et al. 2010; Zu et al. 2011, 2012). This model for AGN continuum variability has been used in a number of other reverberation mapping analyses. For example, Zu et al. (2011) use a CAR(1) process model for the AGN continuum light curve interpolation in their code JAVELIN to measure the time lag between the continuum and an integrated emission line light curve using a top-hat transfer function. Similarly, Li et al. (2013) use a CAR(1) process model in their code to directly model integrated emission line reverberation mapping data based on the BLR model of Pancoast et al. (2011).

In this paper we apply the direct modeling method to the Lick AGN Monitoring Project (LAMP) 2008 reverberation mapping dataset (Walsh et al. 2009; Bentz et al. 2009).[1] The LAMP 2008 campaign observed 13 AGNs using spectroscopy from the Shane Telescope at Lick Observatory and Johnson V and B broad-band photometry from a number of ground-based telescopes. We focused our direct modeling on

---

[1] The LAMP 2008 spectroscopic dataset is available for download here: http://www.physics.uci.edu/~barth/lamp.html

the Hβ line of the 9 objects with measurable time lags, using the broad and narrow Hβ emission line components isolated from the stellar continuum and Fe II lines using spectral decomposition techniques by Park et al. (2012a). Out of the 9 objects to which we applied our direct modeling method, only 5 objects showed sufficient continuum and line variability to allow for constraints on the geometry and dynamics of the BLR. Of the five objects with successful direct modeling of the Hβ line presented here, one of the objects, Arp 151, has previous direct modeling results as described by Brewer et al. (2011a). There are two main differences between the direct modeling of Brewer et al. (2011a) and this work: the first is that we use the spectral decompositions from Park et al. (2012a) instead of Bentz et al. (2009), and the second is that the model of the BLR has since been substantially improved. Improvements to the BLR model include a new dynamics model and two additional geometry model parameters that add flexibility to the shape of the BLR. In addition, we now model the narrow emission line component of Hβ using the width of the [O III]λ5007 narrow emission line and calculate the instrumental resolution for each epoch of spectroscopy separately.

Our focus in this paper is to apply the direct modeling method to the remainder of the LAMP 2008 sample, including reanalysis of Arp 151. In Section 2 we describe the LAMP 2008 data used in our analysis. In Section 3 we briefly review our model for the BLR with further details to be found in a companion paper (Pancoast et al. 2014, hereafter paper I). In Section 4 we present the results of our analysis for the five successfully modeled AGNs in the LAMP 2008 sample. Finally, in Section 5 we summarize our results and discuss their implications for future direct modeling work. All quantities related to properties of the BLR are given in the rest frame of the system.

2 DATA

Our sample of AGNs was observed in the LAMP reverberation mapping campaign in 2008. The first part of the data consists of Johnson B and V broad-band AGN continuum light curves measured using standard aperture photometry techniques, as described by Walsh et al. (2009). The B and V band images were taken at a number of telescopes, including the 30-inch Katzman Automatic Imaging Telescope (KAIT), the 2-m Multicolor Active Galactic Nuclei Monitoring telescope, the Palomar 60-inch telescope, and the 32-inch Tenagra II telescope. For direct modeling of each AGN, we choose to use either the B or V band light curve depending on which has more data points, better sampling of variability features, and higher overall variability. In general, the choice of B or V-band AGN continuum light curve does not change our results.

The second part of the data comprises light curves of broad and narrow Hβ line profiles. Measurement of the Hβ line profiles was done in two ways: Bentz et al. (2009) isolated the Hβ flux by fitting a local linear continuum underneath the Hβ and O III lines, while Park et al. (2012a) applied a multi-component fit to isolate the Hβ line from the AGN continuum, stellar continuum, and Fe II emission lines. Due to the non-negligible contribution of the stellar continuum and Fe emission lines to the five LAMP 2008

objects considered here, we performed direct modeling on the Hβ emission line profiles as measured by Park et al. (2012a). The final spectra we use here for modeling include the broad and narrow Hβ line profiles, as well as the spectral decomposition residuals, equivalent to subtracting off all other components from the original spectrum. The details of the final spectra, including wavelength range used for direct modeling, are given in Table 1.

One other important parameter of the spectral dataset is the instrumental resolution, which is used to smooth the simulated emission line profiles. The instrumental resolution was measured by Bentz et al. (2009, see their Table 11) for four of the five objects by comparing the [O III]λ5007 line widths to the values measured by Whittle (1992). However, there were variations in the [O III]λ5007 line width over the duration of the reverberation mapping campaign due to small changes in the observing and instrumental conditions. For this reason, we calculate the instrumental resolution, $\Delta\lambda_{\mathrm{dis}}$, for each night independently using the width of the [O III]λ5007 line from the spectral decomposition by Park et al. (2012a), $\Delta\lambda_{\mathrm{obs}}$, and the intrinsic line width as measured by Whittle (1992), $\Delta\lambda_{\mathrm{true}}$, by subtracting them in quadrature:

$$\Delta\lambda_{\mathrm{dis}}^2 \approx \Delta\lambda_{\mathrm{obs}}^2 - \Delta\lambda_{\mathrm{true}}^2. \qquad (1)$$

In order to include the uncertainties in these line width measurements, we consider both the measured and intrinsic widths of the [O III]λ5007 line to be free parameters with Gaussian priors centered on the measured values and with dispersions given by the quoted measurement uncertainties. For the one object, SBS 1116+583A, without a comparison line width by Whittle (1992), we use a value in the middle of the range of the values of the other four objects. The values of the intrinsic [O III]λ5007 line width used in this analysis are given in the last column of Table 1 as the line dispersion in Å, converted from the FWHM of the line widths in units of $\mathrm{km\,s^{-1}}$ listed in Whittle (1992) assuming the Gaussian conversion of 2.35, for all objects except SBS 1116+583A.

3 THE DYNAMICAL MODEL OF THE BROAD LINE REGION

In this section we give a brief overview of our simply parameterized phenomenological model of the BLR geometry and dynamics, with full model details given in paper I. We model the distribution of broad line flux emission by the density of many point particles that instantaneously and linearly reprocess the AGN continuum flux and reemit some fraction of it back towards the observer with time lags that depend upon the point particles' positions. The velocities of the point particles then determine how redshifted or blueshifted the broad line flux from the point particles is relative to the systemic velocity of the BLR system. This means that in addition to a model describing the distribution of point particles in position and velocity space, we must also model the AGN continuum flux in order to evaluate it at arbitrary times.

For our model of the AGN continuum light curve we use Gaussian processes, which allows us to sample the AGN continuum variability on scales much smaller than the typical one day cadence between datapoints. This AGN continuum

Table 1. Properties of the LAMP 2008 spectra and photometry. Band is the Johnson broad-band filter. No. Continuum Epochs is the number of data points in the AGN continuum light curve in the band given by column 2. No. Line Epochs is the number of spectra in the broad emission line time series. No. Spectral Pixels is the number of pixels in the Hβ spectrum between the wavelength ranges given in the next column. Wavelengths are in the rest frame. Intrinsic [O III]λ5007 Width is the intrinsic line dispersion σ of the narrow [O III]λ5007 emission line used for calculating the instrumental resolution.

Object	Band	No. Continuum Epochs	No. Line Epochs	No. Spectral Pixels	Wavelength Range (Å)	Intrinsic [O III]λ5007 Width (Å)
Arp 151	B	84	43	73	$4792.3 - 4933.4$	1.562 ± 0.071^a
Mrk 1310	B	50	47	51	$4815.5 - 4913.6$	0.852 ± 0.071^a
NGC 5548	V	57	51	171	$4706.5 - 5040.9$	2.910 ± 0.071^a
NGC 6814	V	46	45	81	$4776.7 - 4935.8$	0.888 ± 0.071^a
SBS 1116+583A	B	56	50	67	$4797.3 - 4925.7$	1.4 ± 0.3

^{a} These values are converted from measurements by Whittle (1992) assuming an uncertainty of $10\,\mathrm{km/s}$.

variability model allows us to include the uncertainty from interpolation in our final uncertainties in the BLR model parameters, as well as allowing us to extrapolate beyond the ends of the light curve in order to evaluate long time lags (for an illustration see Pancoast et al. 2011).

We model the BLR geometry by defining the physical distribution of point particles. The radial distribution is given by a shifted Gamma distribution, which can reproduce Gaussian, exponential or heavy-tailed radial distributions depending on the value of its shape parameter. The point particles are also constrained to be within an (unknown) opening angle, which allows for spherical geometries ranging to thin disk geometries. The BLR is then viewed by an observer with an inclination angle ranging from face-on to edge-on. Finally, there are a number of non-axisymmetric effects that allow for more flexibility in the BLR geometry. These include preferential emission of the point particles from the near or far side of the BLR along the observer's line of sight, a transparent to opaque mid-plane, and the possibility of increased emission from the edges of the BLR disk, relative to the inner portion.

Similarly, we model the BLR dynamics by defining the velocity distribution of point particles as a function of position and black hole mass. We draw the point particles' velocities from distributions in the space of radial and tangential velocities, centered around the circular orbit values or from around the radial escape velocity values for inflowing or outflowing orbits. We allow for a combination of elliptical orbits centered around the circular orbit values plus either inflow or outflow centered around their respective radial escape velocities. To allow for mostly bound inflowing or outflowing orbits, we also allow the distributions of inflowing and outflowing orbits to be centered anywhere along an ellipse between the radial escape velocity and the circular orbit velocity. In order to add more flexibility, we also allow for additional macroturbulent velocities. Finally, we include gravitational redshift and the full expression for doppler shift when moving between the velocities of the point particles and the wavelengths of broad line flux emission. The exact definitions of the geometry and dynamics model parameters are given in Appendix A, with more detailed descriptions given in paper I.

In addition to modeling the broad emission line component using a model for the BLR, we also model the narrow emission line component using the width of the [O III]λ5007

narrow emission line. Since the width of the [O III]λ5007 line is a combination of intrinsic line width and instrumental resolution, we use measurements of the intrinsic line width to constrain the instrumental resolution for smoothing of the broad emission line component.

We explore the parameter space of the BLR model and AGN continuum variability model using Diffusive Nested Sampling (Brewer, Pártay, & Csányi 2011b). This algorithm samples the posterior distribution for the parameters, and provides the "evidence" value which can be used to compare distinct models. We use a Gaussian likelihood function that compares the time series of broad emission line profiles of the data to the simulated versions generated by our BLR model. Since the model is of finite flexibility and the spectral data have high signal to noise and a large number of data points, it is necessary to soften the likelihood function. We do this by defining a temperature T by which the log of the likelihood is divided, where $T \geqslant 1$. Temperatures greater than one can be thought of as an additional source of uncertainty in the likelihood due to the model not providing a perfect fit to the data, either because the error bars of the data are underestimated or because the model does not contain enough complexity to reproduce all features of the data. The use of a temperature can be thought of as a computationally inexpensive approximation to a correlated noise model. Since we use Nested Sampling, the choice of temperature T can be made in post-processing and does not require multiple runs.

4   RESULTS

We now present the results of direct modeling of five AGNs in the LAMP 2008 sample, including Arp 151, Mrk 1310, NGC 5548, NGC 6814, and SBS 1116+583A. First, the modeling results are presented in detail for each AGN, including key posterior PDFs and correlations, the model fit to the data, and the transfer function. Examples of the inferred geometry of the BLR for each AGN are also shown in Figure 1 and the AGN continuum light curves with Gaussian process interpolations drawn from the posterior are shown in Figure 2. The posterior median and central 68% credible intervals for the main BLR model parameters are given in Table 2. Second, we present an overview of the BLR modeling results to emphasize the similarities and differences in
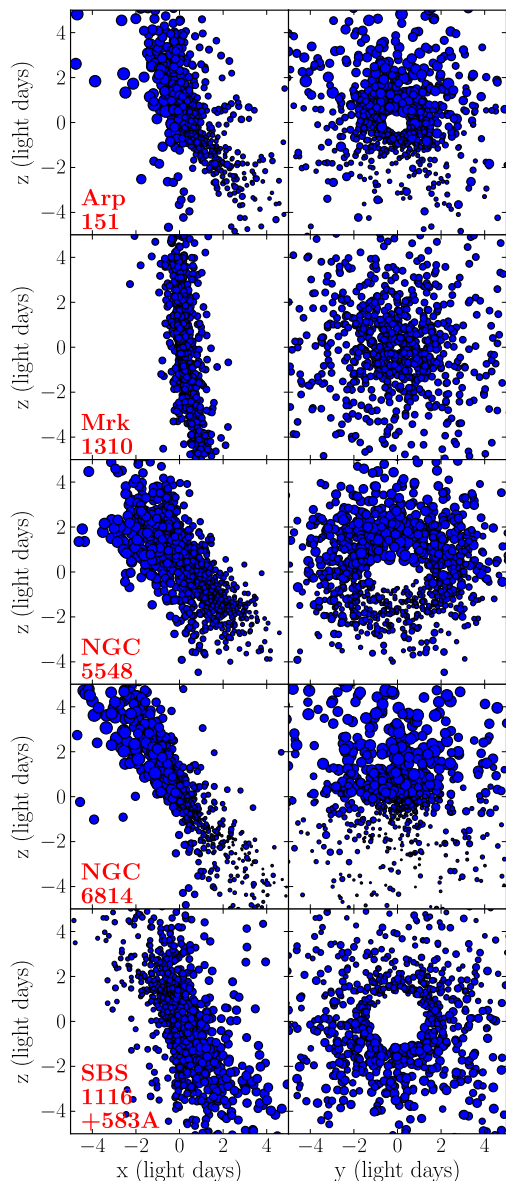
Figure 1. Geometries of the BLR for the five objects in our sample. The left panels show the BLR from along the y axis (the edge-on view), while the right panels show the BLR from along the positive x axis (the observer's point of view). Top to bottom: Arp 151, Mrk 1310, NGC 5548, NGC 6814, and SBS 1116+583A. Each point corresponds to a point particle in our BLR model and the size of the points is proportional to the relative amount of Hβ emission coming from each point particle, given the same incident continuum flux.

Figure 2. AGN continuum light curves for the five objects in our sample. The data are shown by black points with error bars and the Gaussian process interpolations drawn from the posterior PDF are shown by the colored lines. Top to bottom: Arp 151, Mrk 1310, NGC 5548, NGC 6814, and SBS 1116+583A.

the sample. Finally, we calculate the mean f factor for this sample of five AGNs.

4.1 Individual Modeling Results

4.1.1 Arp 151 (Mrk 40)

Both the AGN continuum and broad Hβ line showed strong variability over the duration of the LAMP 2008 campaign, leading to the clearest velocity-resolved lag measurements of the LAMP 2008 sample (Bentz et al. 2009) and the most de-

tailed transfer function recovered at the time using MEME-CHO (Bentz et al. 2010). It is therefore unsurprising that the direct modeling results for Arp 151 also have the highest quality of the LAMP 2008 sample.

Comparison of the spectral time series and time series of simulated spectra, as illustrated in Figure 3, suggests that the model is able to fit the overall variability structure of the Hβ line profile very well. In addition, the integrated model Hβ emission line and individual model spectra show excellent agreement. The model is unable to capture very short timescale variations that are either due to noise or processes with much faster response times than the overall variability of the BLR would suggest. Fortunately, such short timescale variations are infrequent and do not appear to substantially affect inference of the model parameters.

The geometry of the BLR in Arp 151 as traced by Hβ emission is inferred to be a wide thick disk, inclined by $\theta_i = 25.2^{+3.3}_{-3.4}$ degrees relative to the observer (0 = face-on). The radial distribution of Hβ emission has heavier tails than an exponential profile, with a Gamma distribution shape parameter of $\beta = 1.25^{+0.15}_{-0.16}$, mean radius $r_{\mathrm{mean}} = 3.44^{+0.26}_{-0.24}$
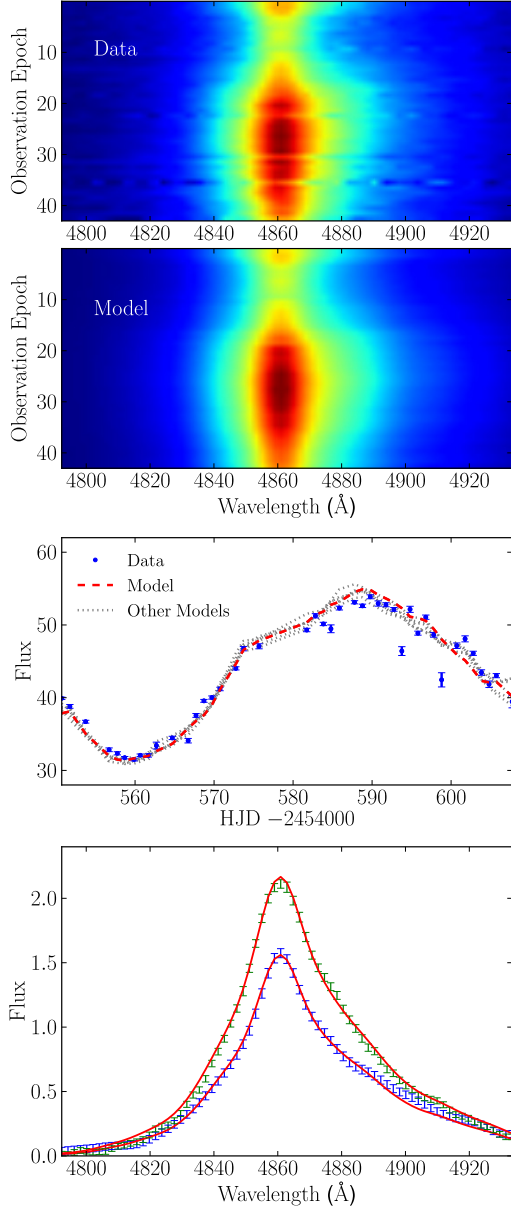
Figure 4. Marginal posterior PDFs and correlations between parameters for Arp 151, including black hole mass (M_{BH}), inclination angle (θ_i), and opening angle (θ_o).

days by Bentz et al. (2009) to within the uncertainties. Due to the heavy tails of the radial profile, the median lag of $\tau_{median} = 1.75^{+0.28}_{-0.23}$ days is significantly shorter. The opening angle of the disk is well constrained to be $\theta_o = 25.6^{+3.7}_{-4.0}$ degrees, however more emission is found to come from the outer faces of the disk ($\gamma = 4.27^{+0.54}_{-0.80}$), making the geometry closer to a cone. There is also preferential emission from the far side of the BLR from the observer ($\kappa = -0.36^{+0.08}_{-0.08}$) and the mid-plane of the BLR disk is found to be mostly opaque ($\xi = 0.09^{+0.08}_{-0.05}$). An example of the BLR geometry in Arp 151 for a set of model parameters drawn from the posterior is shown in Figure 1.

The dynamics of the BLR in Arp 151 are inferred to be dominated by inflowing orbits, with the fraction of point particles in elliptical orbits only $f_{ellip} = 0.06^{+0.09}_{-0.05}$, or $1 - 15\%$. The majority of the point particles are in inflowing orbits as given by the inflow/outflow parameter $f_{flow} = 0.24^{+0.20}_{-0.17}$, where values of f_{flow} between 0 and 0.5 indicate inflow and values between 0.5 and 1 indicate outflow. Comparing the probability for values of f_{flow} between 0 and 0.5 with the probability for values between 0.5 and 1 indicates a 100% preference for inflow compared to outflow. Furthermore, the inferred inflowing orbits are not strictly radial or drawn from a velocity distribution centered on the radial escape velocity, but can be distributed closer to the circular orbit value, leading to more bound inflowing orbits. The value of $\theta_e = 12.0^{+10.7}_{-8.3}$ that we infer for Arp 151 indicates that the inflow orbit velocity distribution is rotated about a seventh of the way towards the circular-orbit-centered distribution and that more than half of the inflowing orbits are bound. Finally, we find a negligible contribution to the dynamics of the BLR from macroturbulent velocities, with the dispersion of additional macroturbulent velocities drawn from a

Figure 3. Model fit to the broad and narrow Hβ line dataset for Arp 151. Top panel: the Hβ spectral time series of data from Park et al. (2012a). Top middle panel: an example of a simulated Hβ spectral time series for a model drawn randomly from the posterior PDF. Bottom middle panel: the integrated Hβ line light curve with data from Park et al. (2012a) given by the blue points with error bars, the model in the top middle panel shown with the red dashed line, and additional models drawn from the posterior shown with the dotted grey lines. Bottom panel: two examples of the Hβ line profile shown with blue and green error bars with the model fits over-plotted with red lines.

light days, and dispersion or radial width of $\sigma_r = 3.72^{+0.45}_{-0.43}$ light days. The radial distribution is offset from the origin, the source of the ionizing photons and visible continuum emission, by $r_{min} = 0.44^{+0.13}_{-0.20}$ light days. The mean radius equals to within the uncertainties the mean lag of $\tau_{mean} = 3.07^{+0.25}_{-0.20}$ days, which in turn is consistent with the cross-correlation measured central lag of $\tau_{cent} = 3.99^{+0.49}_{-0.68}$
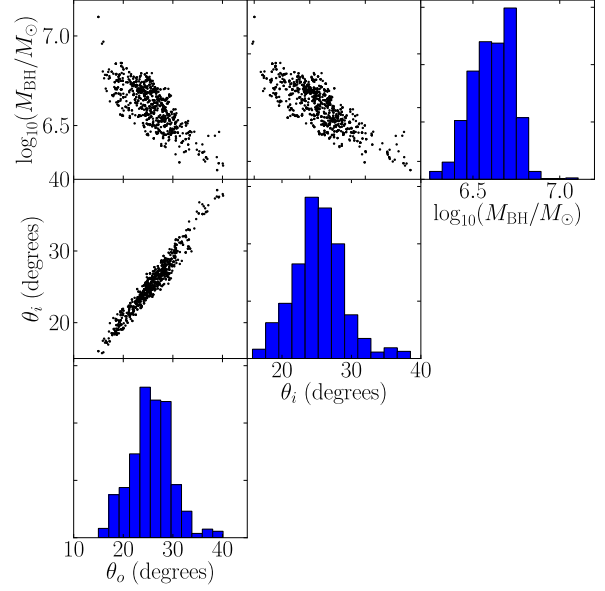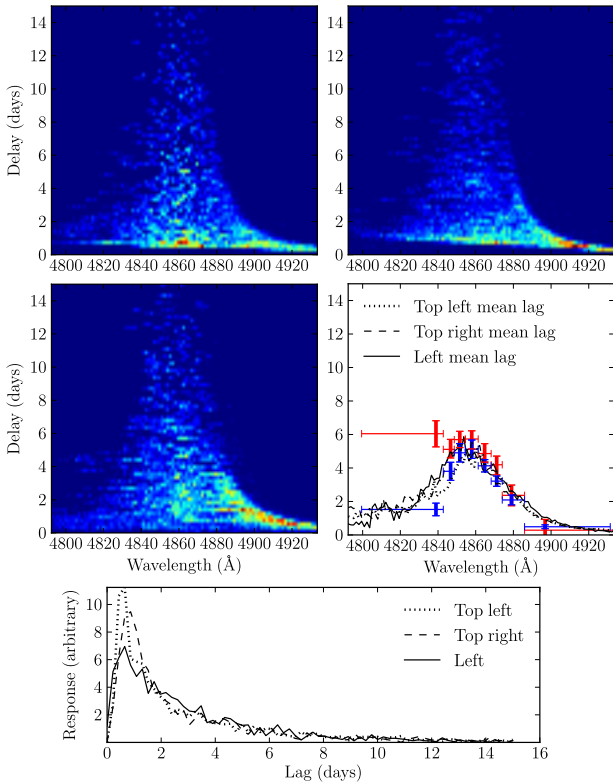
Figure 5. Transfer functions for Arp 151. The top two panels and the middle left panel are all examples of transfer functions drawn from the posterior PDF of the model fit. The middle right panel shows the mean lag as a function of velocity for each of the three transfer functions from the posterior. Also shown in this panel are the velocity-resolved cross-correlation lag measurements from Bentz et al. (2009) as red error bars, where the horizontal error bars show the wavelength ranges used in the integrated light curves. Our mean lag values in these same bins are shown by the blue error bars, except for the longest wavelength bin which does not extend as far to the red as the one by Bentz et al. (2009). The bottom panel shows the velocity-integrated transfer function for each of the three transfer functions from the posterior.

Hβ line width after spectral decomposition from Park et al. (2012a) to construct two sets of virial products. The first type of virial product uses the line dispersion measured from the RMS line profile as the Hβ line width and the second uses the FWHM of the mean line profile as the Hβ line width. Values of the f factor calculated using the first type of virial product will be referred to as f_σ, while values calculated using the second type of virial product will be referred to as $f_{\rm FWHM}$. We obtain the distribution of f for each AGN by subtracting the virial product from the normalized posterior PDF of black hole mass. The inferred f factors for the five AGNs in our sample are listed in Table 3. For Arp 151, we measure f factors of $\log_{10}(f_\sigma) = 0.51^{+0.10}_{-0.13}$ and $\log_{10}(f_{\rm FWHM}) = -0.24^{+0.10}_{-0.13}$.

Previous direct modeling results for Arp 151 constrained the black hole mass to be $10^{6.51\pm0.28}\,M_\odot$ and the geometry to be a wide thick disk with an opening angle of $\theta_o = 34.5^{+10.7}_{-8.6}$ degrees, inclined with respect to the observer by $\theta_i = 22.2 \pm 7.8$ degrees (Brewer et al. 2011a). Our improved modeling results for Arp 151 are completely consistent to within the uncertainties with these previous modeling results, and clarify the previous ambiguity in whether the dynamics of Hβ in Arp 151 are dominated by inflow or outflow.

For comparison with work focused on recovering the velocity-resolved transfer function, we show three transfer functions created from models drawn randomly from the multi-dimensional posterior PDF in Figure 5. While the three transfer functions show slightly different detailed structure, the mean lag as a function of velocity is very similar for all three, as is the velocity-integrated transfer function. In addition, all three velocity-resolved transfer functions show at least some preference for prompt response on the red side of the line profile, indicative of inflow kinematics. The same inflow signatures were found in the transfer function recovered using MEMECHO (Bentz et al. 2010), as well as the velocity-resolved lag measurements, shown in red in the middle right panel of Figure 5. The discrepancy in the blue wing of the line between the velocity-resolved lag measurements from CCF analysis (in red in Figure 5) and dynamical modeling (in blue) is due to a combination of data preprocessing and systematics from measurement of the time lag. Recalculating the velocity-resolved time lags from CCF analysis using the same datasets as in the dynamical modeling decreased the discrepancy in the bluest lag bin by ~ 1.5 days while remaining consistent with the values from Bentz et al. (2009). The remaining discrepancy is due to the difference between the true mean time delay and the time delay proxy estimated by CCF analysis. We confirm this by creating velocity-resolved light curves using the inferred models of the BLR for Arp 151, calculating and showing that the CCF time lag from those model light curves and the time lags from dynamical modeling are consistent with the values from Bentz et al. (2009). However there are residual differences between the transfer functions from direct modeling and MEMECHO, including response in the blue wing of the line, where direct modeling finds significantly shorter lags, and prompt response of the line emission at line center, where the MEMECHO solution finds no prompt response.
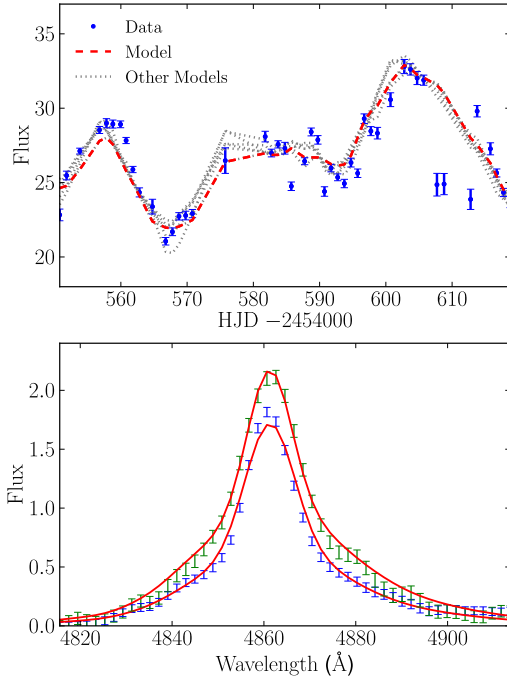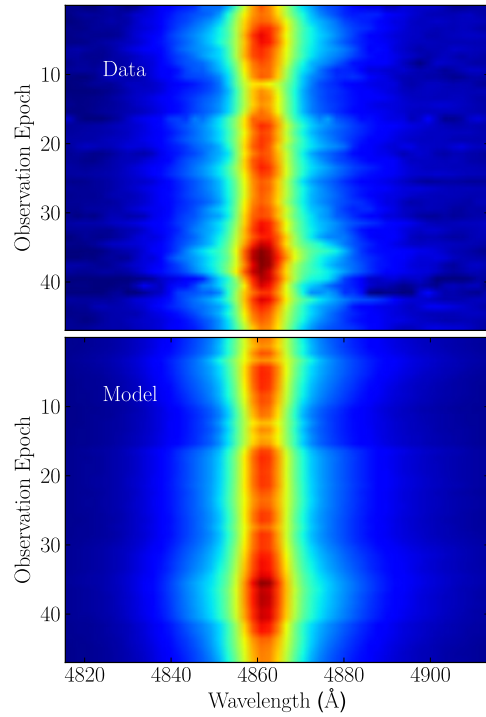
Gaussian distribution of only $\sigma_{\rm turb} = 0.008^{+0.028}_{-0.007}$ times the circular orbit velocity.

We measure a black hole mass for Arp 151 of $\log_{10}(M_{\rm BH}/M_\odot) = 6.62^{+0.10}_{-0.13}$. As illustrated in Figure 4, there is strong degeneracy between the black hole mass, inclination angle, and opening angle, preventing us from measuring the black hole mass with greater precision. The correlation between these parameters is easy to understand if one considers that the BLR model parameters are constrained such that the line-of-sight velocity matches the width of the emission line: for thin disks, the more face-on the BLR, the higher the black hole mass must be to produce the same line-of-sight velocities. The opening angle is also strongly correlated, since a thicker disk allows for larger line-of-sight velocities for a given black hole mass.

With an independent measurement of the black hole mass we can use the virial product $M_{\rm vir}$ from traditional reverberation mapping analysis to measure the f factor for Arp 151. We use the time lags $\tau_{\rm cent}$ from cross-correlation analysis from Bentz et al. (2009) and measurements of the

Figure 7. Same as Figure 4, but for Mrk 1310.

Figure 6. Same as Figure 3, but for Mrk 1310.

Figure 8. Same as Figure 5, but for Mrk 1310.

4.1.2   Mrk 1310

With the narrowest Hβ line profile in our sample, the dataset for Mrk 1310 provides fewer constraints on the BLR model due to a smaller number of pixels per spectrum and reduced variability compared to Arp 151. Despite these issues, the model is able to match the overall variability of the emission line profile, as well as the detailed line profile shape, as shown in Figure 6.
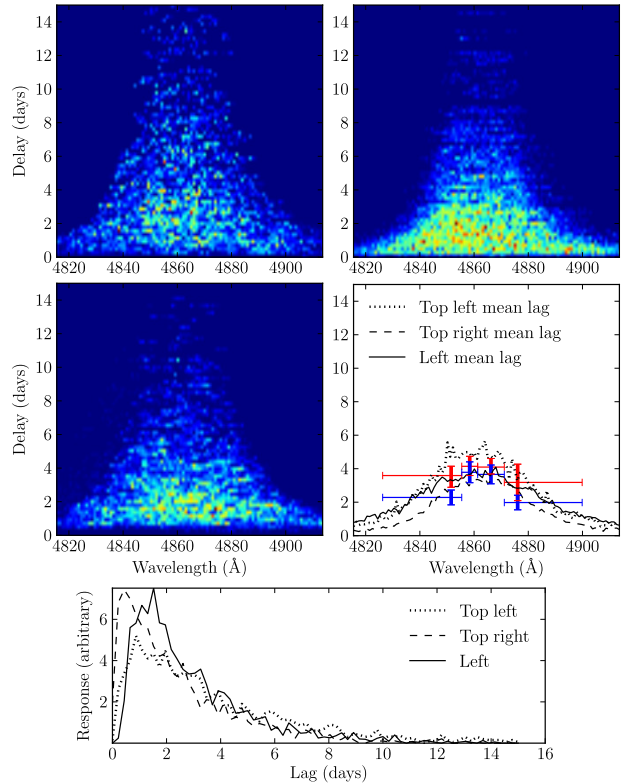
The geometry of the Hβ BLR for Mrk 1310 is con-

strained to be a thick disk, inclined by $\theta_i = 6.6^{+5.0}_{-2.5}$ degrees with respect to the observer, although inclination angles up to 35 degrees are not completely ruled out. The radial distribution of Hβ emission is constrained to be between exponential and Gaussian ($\beta = 0.89^{+0.10}_{-0.10}$), with a mean radius of $r_{\mathrm{mean}} = 3.13^{+0.42}_{-0.40}$ light days, a minimum radius away from the central source of ionizing photons of $r_{\mathrm{min}} = 0.12^{+0.19}_{-0.08}$ light days, and a radial dispersion or width of $\sigma_r = 2.59^{+0.42}_{-0.35}$ light days. The mean time lag of $\tau_{\mathrm{mean}} = 2.96^{+0.42}_{-0.35}$ days is very similar to the mean radius and median time lag of $\tau_{\mathrm{median}} = 2.26^{+0.35}_{-0.31}$, and agrees to within the uncertainties with the cross-correlation lag of $\tau_{\mathrm{cent}} = 3.66^{+0.59}_{-0.61}$ days measured by Bentz et al. (2009). The opening angle of the disk is inferred to be $\theta_o = 8.6^{+3.5}_{-2.1}$ degrees, although opening angles up to 35 degrees are not completely ruled out. There is no preference for Hβ emission from the outer faces of the BLR disk ($\gamma = 2.97^{+1.38}_{-1.43}$), for emission from the far or near side of the BLR ($\kappa = -0.04^{+0.38}_{-0.35}$) or for the transparency of the BLR midplane ($\xi = 0.40^{+0.38}_{-0.29}$). An illustration of the BLR geometry for Mrk 1310 is shown in Figure 1 for one sample from the posterior PDF.

The dynamics of the BLR for Mrk 1310 are unclear. There is a slight preference for elliptical orbits ($f_{\mathrm{ellip}} = 0.56^{+0.34}_{-0.39}$) and placement of the inflowing/outflowing velocity distribution closer to the distribution centered on the circular orbit value ($\theta_e = 57.2^{+24.9}_{-41.0}$ degrees), but also a preference for the remaining orbits to be outflowing when $\theta_e \to 90$ degrees ($f_{\mathrm{flow}} = 0.65^{+0.24}_{-0.38}$, probability of inflow/outflow is 31%/69%). This shows that radial outflowing orbits are not actually strongly preferred compared to radial inflowing orbits and the dynamics of the BLR are not well-constrained in this case. We also find no preference for substantial macroturbulent velocities ($\sigma_{\mathrm{turb}} = 0.004^{+0.010}_{-0.003}$).

The black hole mass for Mrk 1310 is inferred to be $\log_{10}(M_{\mathrm{BH}}/M_\odot) = 7.42^{+0.26}_{-0.27}$. The uncertainty in the black hole mass is due in large part to degeneracy with the inclination angle and opening angle, as shown in Figure 7, since at very small inclination and opening angles large changes in black hole mass are needed to maintain the line-of-sight velocity of the point particles for even small changes in inclination or opening angle. Comparing our measurement of the black hole mass to the virial products calculated from cross-correlation time lags from Bentz et al. (2009) and line widths from Park et al. (2012a), we measure the f factors for Mrk 1310 to be $\log_{10}(f_\sigma) = 1.63^{+0.26}_{-0.27}$ and $\log_{10}(f_{\mathrm{FWHM}}) = 0.79^{+0.26}_{-0.27}$ (see Section 4.1.1).

The velocity-resolved transfer functions for Mrk 1310, drawn randomly from the posterior PDF, show very similar structure as illustrated in Figure 8, despite ambiguity in the dynamics of the BLR. The mean velocity-resolved transfer functions and the velocity-integrated transfer functions also show very similar features, and agree to within the uncertainties with the cross-correlation velocity-resolved lag measurements from Bentz et al. (2009).

4.1.3 NGC 5548

While not as variable as Arp 151 over the duration of the LAMP 2008 campaign, the NGC 5548 Hβ line profile is the widest in the sample, providing an informative dataset with which to constrain the BLR model. The model is able to fit

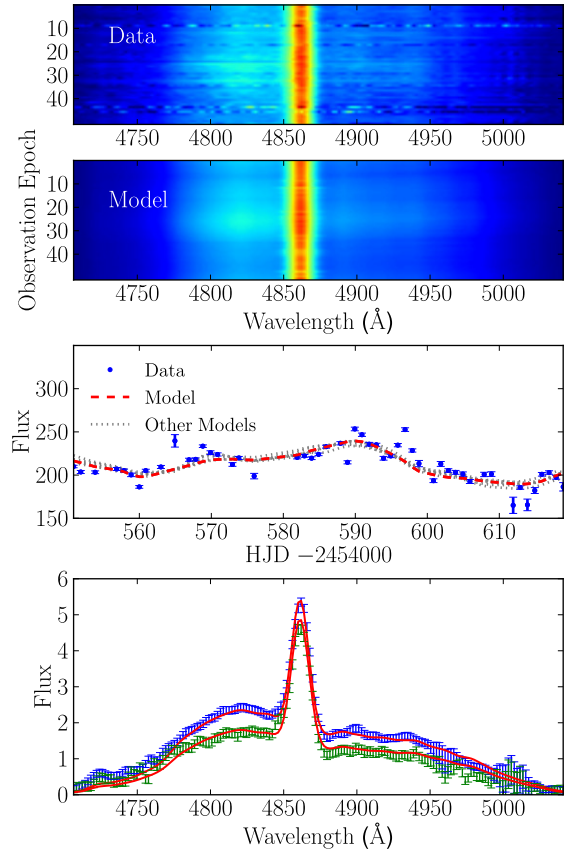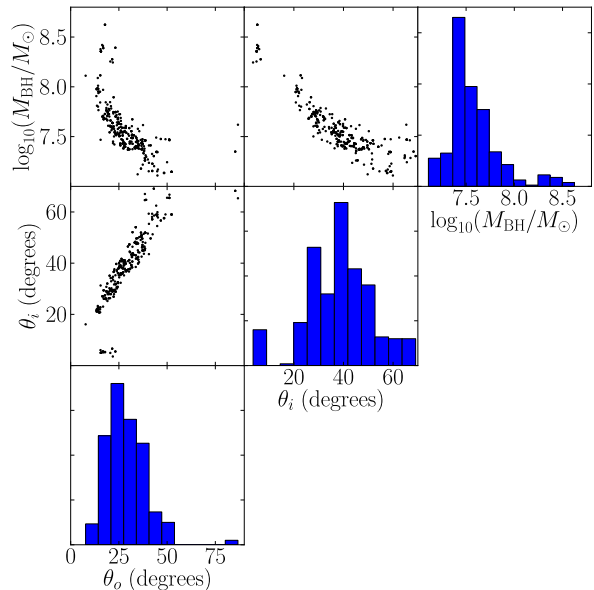**Figure 9.** Same as Figure 3, but for NGC 5548.

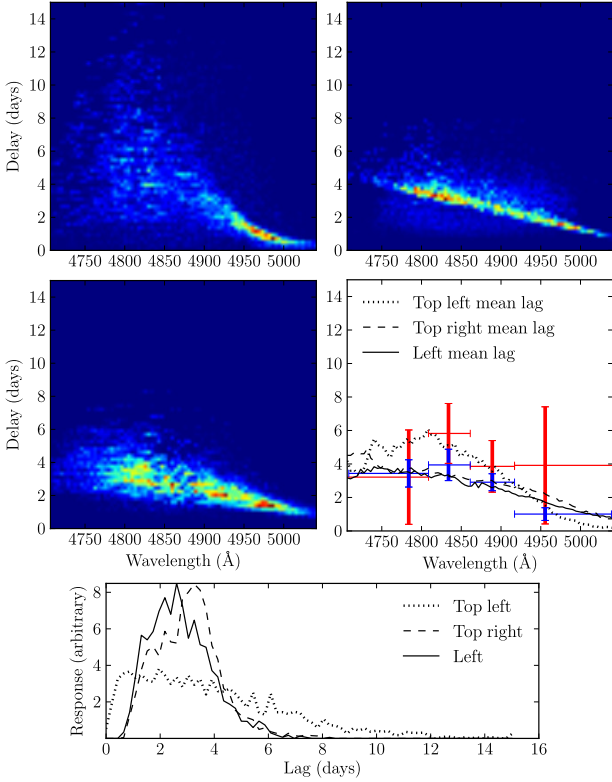**Figure 10.** Same as Figure 4, but for NGC 5548.

Figure 11. Same as Figure 5, but for NGC 5548.

the overall variability of the Hβ line profile as well as the detailed emission line shape, as shown in Figure 9.

The geometry of the Hβ BLR in NGC 5548 is constrained to be a narrow thick disk, with an inclination angle of $\theta_i = 38.8^{+12.1}_{-11.4}$ degrees. The radial distribution of Hβ emission is between exponential and Gaussian ($\beta = 0.80^{+0.60}_{-0.31}$), with a mean radius of $r_{\rm mean} = 3.31^{+0.66}_{-0.61}$ light days, a minimum radius from the central ionizing source of $r_{\rm min} = 1.39^{+0.80}_{-1.01}$ light days, and a dispersion or width of the BLR of $\sigma_r = 1.50^{+0.73}_{-0.60}$ light days. The mean lag is very similar to the mean radius, with $\tau_{\rm mean} = 3.22^{+0.66}_{-0.54}$ days, and consistent to within the uncertainties with the cross-correlation lag measurement of $\tau_{\rm cent} = 4.17^{+0.90}_{-1.33}$ by Bentz et al. (2009). The median lag is smaller with $\tau_{\rm median} = 2.77^{+0.63}_{-0.42}$ days. The opening angle of the disk is inferred to be $\theta_o = 27.4^{+10.6}_{-8.4}$ degrees with opening angles near 90 degrees not completely ruled out and with a slight preference for emission equally concentrated throughout the disk ($\gamma = 2.01^{+1.78}_{-0.71}$). The H$\beta$ emission is also found to preferentially emit from the far side of the BLR ($\kappa = -0.24^{+0.06}_{-0.13}$) and the midplane of the BLR is found to be not fully transparent ($\xi = 0.34^{+0.11}_{-0.18}$). An example of the BLR geometry in NGC 5548 is shown in Figure 1 for a single posterior sample.

The dynamics of the BLR in NGC 5548 are found to be mostly inflow. The fraction of point particles with elliptical orbits is $\sim 10 - 40\%$ ($f_{\rm ellip} = 0.23^{+0.15}_{-0.15}$), with the rest of the point particles favoring inflowing orbits ($f_{\rm flow} = 0.25^{+0.21}_{-0.16}$, probability of inflow/outflow is 94%/6%). Like in the case of Arp 151, the inferred inflowing orbits are mostly bound, with the inflow velocity distribution rotated towards the elliptical orbit distribution by $\theta_e = 21.3^{+21.4}_{-14.7}$ degrees in the

radial and tangential velocities plane. There is also minimal contribution from additional macroturbulent velocities ($\sigma_{\rm turb} = 0.016^{+0.044}_{-0.013}$).

We measure the black hole mass in NGC 5548 to be $\log_{10}(M_{\rm BH}/M_\odot) = 7.51^{+0.23}_{-0.14}$. Similar to Arp 151 and Mrk 1310, there are strong correlations between the black hole mass, inclination angle, and opening angle that contribute to the uncertainty in black hole mass, as shown in Figure 10. By comparing our measurement of the black hole mass to the virial products calculated from cross-correlation time lags from Bentz et al. (2009) and line widths from Park et al. (2012a), we measure the f factors for NGC 5548 to be $\log_{10}(f_\sigma) = 0.42^{+0.23}_{-0.14}$ and $\log_{10}(f_{\rm FWHM}) = -0.58^{+0.23}_{-0.14}$ (see Section 4.1.1).

The velocity-resolved transfer functions randomly chosen from the posterior show a variety of structures consistent with inflow, as shown in Figure 11. However, the mean lags for the velocity-resolved transfer functions and the velocity-integrated transfer functions are not completely consistent. Despite this, the velocity-resolved lag measurements by Bentz et al. (2009) are consistent to within the uncertainties with our mean lag estimates, suggesting that we are able to constrain the general shape of the transfer function if not the detailed structure.

4.1.4 NGC 6814

While the model is able to capture the detailed line profile shape for NGC 6814, it has more difficulty matching the overall variability of the Hβ emission, as illustrated in Figure 12. The integrated Hβ light curves show some discrepancy, especially at early times, and the second bright peak in the spectra is not as strong in the model.

For this object, the BLR as traced by Hβ emission is constrained to be a wide thick disk, inclined by $\theta_i = 49.4^{+20.4}_{-22.2}$ degrees with respect to the line of sight, where inclination angles approaching 90 degrees are not ruled out. The radial distribution of Hβ emission is close to exponential ($\beta = 1.07^{+1.15}_{-0.09}$), with a mean radius of $r_{\rm mean} = 3.76^{+1.15}_{-0.77}$ light days, a minimum radius from the central ionizing source of $r_{\rm min} = 0.15^{+0.19}_{-0.11}$ light days, and a dispersion or width of the BLR of $\sigma_r = 3.75^{+1.05}_{-0.69}$ light days. The mean radius is close to the mean time lag of $\tau_{\rm mean} = 4.43^{+0.72}_{-0.83}$ days, which is marginally consistent with the cross-correlation lag of $\tau_{\rm cent} = 6.46^{+0.94}_{-0.96}$ by Bentz et al. (2009). The median lag is considerably shorter, with $\tau_{\rm median} = 2.67^{+0.60}_{-0.61}$. The opening angle of the disk is inferred to be $\theta_o = 50.2^{+22.0}_{-18.6}$ degrees, and a spherical geometry is not ruled out. While there is no preference for concentrated Hβ emission from the edges of the disk ($\gamma = 2.91^{+1.37}_{-1.31}$), there is a slight preference for the disk midplane to be transparent ($\xi = 0.71^{+0.22}_{-0.33}$) and a strong preference for concentration of Hβ emission from the far side of the BLR ($\kappa = -0.44^{+0.10}_{-0.05}$), although more emission from the near side is not completely ruled out. The BLR geometry for NGC 6814 from one posterior sample is illustrated in Figure 1.

The dynamics of the BLR for NGC 6814 are inferred to be a combination of elliptical and inflowing orbits. The fraction of elliptical orbits ranges between $0 - 70\%$ ($f_{\rm ellip} = 0.32^{+0.17}_{-0.22}$), with the remainder of the orbits mostly inflowing ($f_{\rm flow} = 0.29^{+0.25}_{-0.19}$, probability for inflow/outflow is 83%/17%). For the inflowing/outflowing orbits where the

Figure 12. Same as Figure 3, but for NGC 6814.

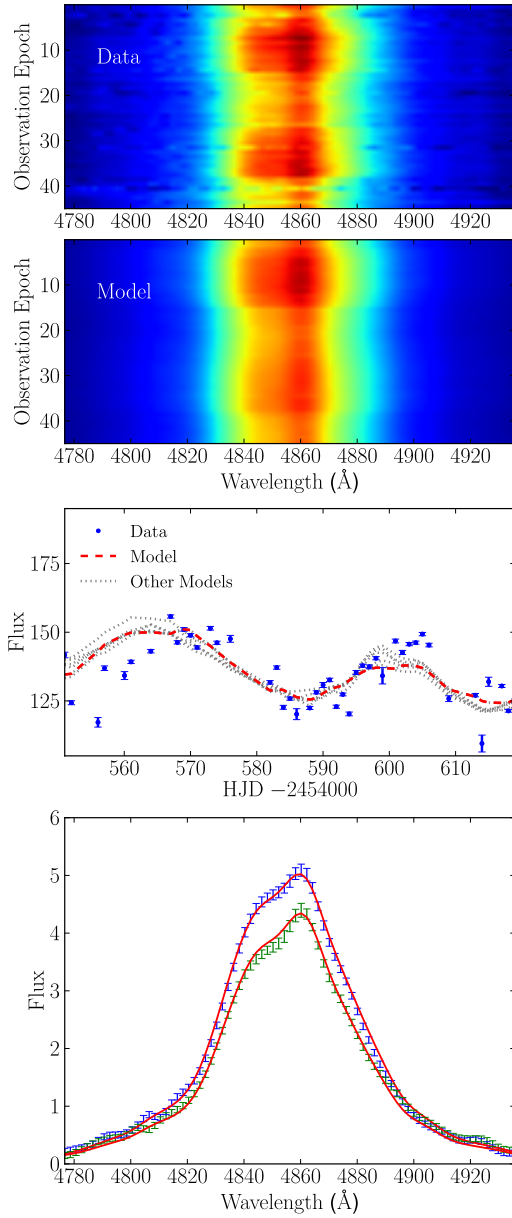**Figure 13.** Same as Figure 4, but for NGC 6814.

Figure 14. Same as Figure 5, but for NGC 6814.

fraction of elliptical orbits is small, the distribution of inflowing/outflowing velocities is rotated by ~ 60 degrees towards the elliptical orbit distribution in the radial and tangential velocity plane ($\theta_e \sim 60$). This means that in the majority of inferred model solutions with low fractions of elliptical orbits, the inflowing orbits are bound and more similar to circular orbits in terms of tangential versus radial velocity component magnitudes. For the full set of posterior model solutions, $\theta_e = 47.0^{+16.7}_{-26.5}$. Finally, there is minimal contribution from additional macroturbulent velocities ($\sigma_{\text{turb}} = 0.013^{+0.036}_{-0.011}$).

We measure the black hole mass in NGC 6814 to be $\log_{10}(M_{\text{BH}}/M_\odot) = 6.42^{+0.24}_{-0.18}$. The correlations of inclination angle and opening angle with black hole mass are not as tight for this object, adding less uncertainty to the inference of black hole mass, as shown in Figure 13. By comparing our
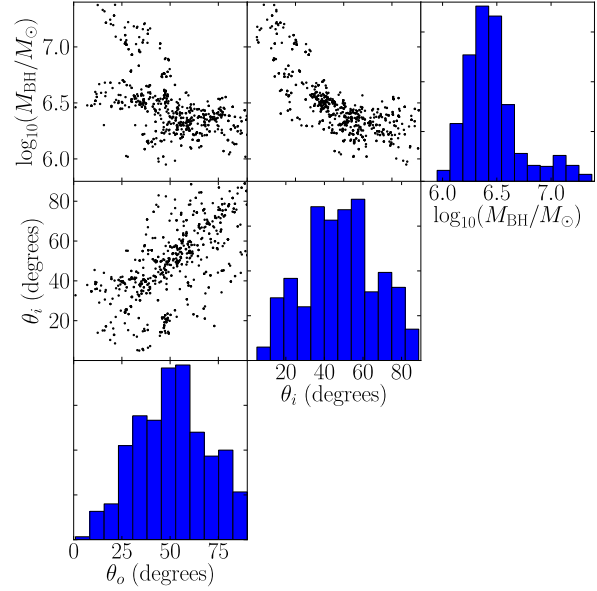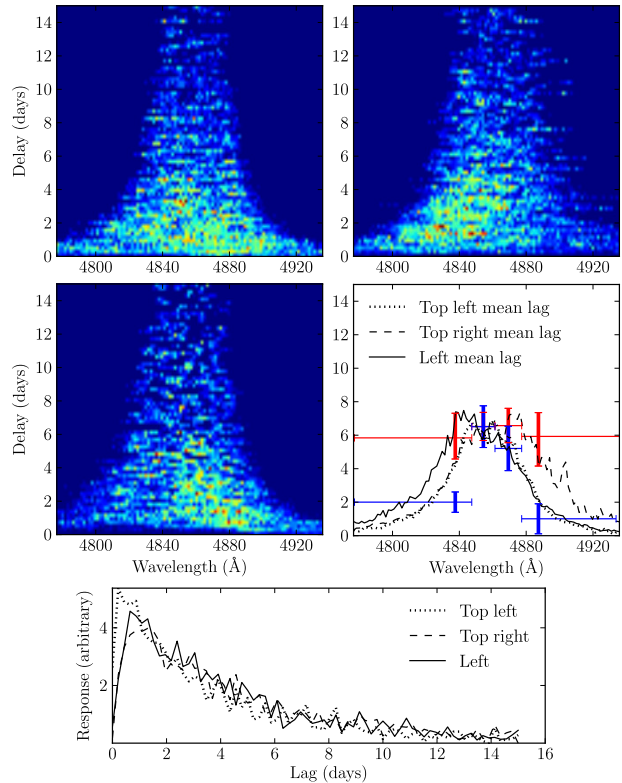
measurement of the black hole mass to the virial products calculated from cross-correlation time lags from Bentz et al. (2009) and line widths from Park et al. (2012a), we measure the f factors for NGC 6814 to be $\log_{10}(f_\sigma) = -0.14^{+0.24}_{-0.18}$ and $\log_{10}(f_{\mathrm{FWHM}}) = -0.68^{+0.24}_{-0.18}$ (see Section 4.1.1).

The velocity-resolved transfer functions drawn randomly from the posterior show similar overall structure, as shown in Figure 14, although an excess of response in the blue wing, red wing, or center of the line changes between samples. The line wings also generally have shorter lags than suggested by the velocity-resolved lag measurements by Bentz et al. (2009). As for Arp 151, this discrepancy is due to the method of measuring the time lag. Again, we confirm this by creating velocity-resolved light curves using the inferred models of the BLR for NGC 6814 and comparing the CCF time lag measured from these model light curves to the CCF time lags from Bentz et al. (2009). In this case, the comparison is not conclusive. Owing to the low signal-to-noise ratio of the data in the wings of the line, the cross-correlation results are very uncertain, and depend significantly upon the details of the CCF calculation, such as the interval over which the CCF is calculated. Despite this, the velocity-integrated transfer functions are consistent, suggesting that the general shape of the velocity resolved transfer function is well constrained.

4.1.5   SBS 1116+583A

The model fits to SBS 1116+583A capture the overall variability of the data and successfully match the Hβ line profile shape, as shown in Figure 15. We infer the geometry for the BLR in this object to be a wide, thick disk inclined by $\theta_i = 18.2^{+8.4}_{-5.9}$ degrees with respect to the line of sight, although inclination angles approaching 90 degrees are not ruled out. The radial distribution of Hβ emission is constrained to be close to exponential ($\beta = 1.00^{+0.27}_{-0.21}$). The mean radius is $r_{\mathrm{mean}} = 4.07^{+0.79}_{-0.65}$ light days, the minimum radius from the central ionizing source is $r_{\mathrm{min}} = 0.93^{+0.50}_{-0.49}$ light days, and the radial dispersion or width of the BLR is $\sigma_r = 3.14^{+0.81}_{-0.66}$ light days. The mean radius agrees well with the mean lag of $\tau_{\mathrm{mean}} = 3.78^{+0.57}_{-0.52}$ days, which is marginally consistent to within the uncertainties with the cross-correlation lag of $\tau_{\mathrm{cent}} = 2.31^{+0.62}_{-0.49}$ days (Bentz et al. 2009). In this case the cross-correlation lag is closer to the median time lag of $\tau_{\mathrm{median}} = 2.71^{+0.40}_{-0.37}$ days. The opening angle of the disk is inferred to be $\theta_o = 21.7^{+11.0}_{-7.5}$ degrees, and opening angles approaching 90 degrees, corresponding to spherical geometries, are not ruled out. The other parameters of the BLR geometry model are unconstrained, including emission from the front or back side of the BLR ($\kappa = -0.03^{+0.31}_{-0.34}$), preferential emission from the faces of the disk ($\gamma = 3.19^{+1.21}_{-1.37}$), and the transparency of the disk mid-plane ($\xi = 0.61^{+0.28}_{-0.37}$).

The dynamics of the BLR are inferred to be dominated by elliptical orbits. The elliptical orbit fraction is $f_{\mathrm{ellip}} = 0.66^{+0.21}_{-0.27}$. The remaining orbits are mostly inflowing ($f_{\mathrm{flow}} = 0.31^{+0.31}_{-0.22}$, probability of inflow/outflow is 79%/21%). When the elliptical orbit fraction drops below $\sim 50\%$ then the majority of inflow or outflow solutions have $\theta_e > 50$ degrees, so the inflow or outflow velocity distributions are rotated in the radial and tangential velocity plane towards the elliptical orbit distribution. This is compared
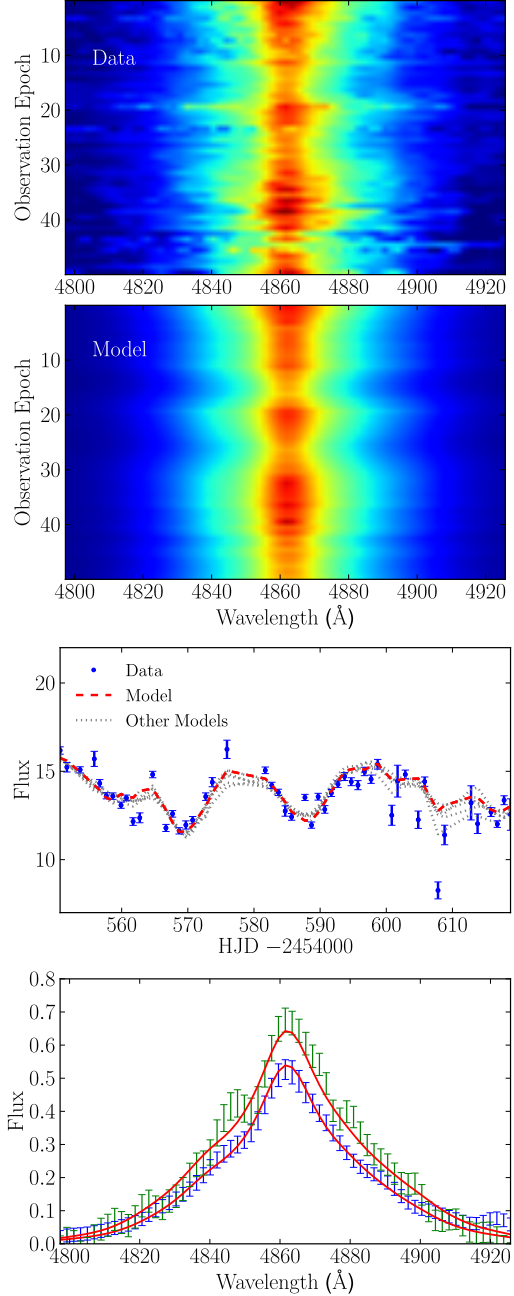

Figure 15. Same as Figure 3, but for SBS 1116+583A.

to $\theta_e = 49.7^{+28.8}_{-32.1}$ degrees for the full posterior. This means that even posterior samples with a majority of point particle velocities drawn from the inflow or outflow velocity distributions have mainly elliptical-like orbits. Finally, the dynamics in SBS 1116+583A is inferred to have minimal contribution from macroturbulent velocities with $\sigma_{\mathrm{turb}} = 0.011^{+0.033}_{-0.009}$ in units of the circular velocity.

We measure the black hole mass in SBS 1116+583A to be $\log_{10}(M_{\mathrm{BH}}/M_\odot) = 6.99^{+0.32}_{-0.25}$. There is a strong correlation between black hole mass and inclination angle and opening angle, as shown in Figure 16. Comparing our measurement of the black hole mass to the virial products cal-
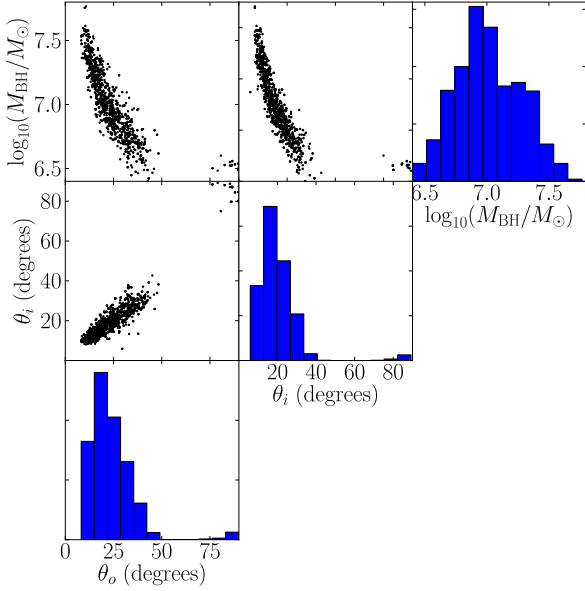
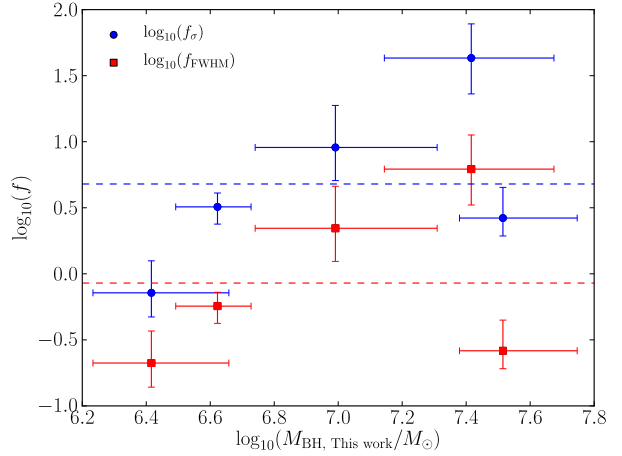**Figure 18.** Individual f factors versus black hole mass as inferred by direct modeling. The blue circles show the values of $\log_{10}(f_\sigma)$, while the red squares show the values of $\log_{10}(f_{\rm FWHM})$. The values of $\langle\log_{10}(f_\sigma)\rangle$ and $\langle\log_{10}(f_{\rm FWHM})\rangle$ for the sample are shown by the top blue and bottom red dashed lines, respectively.

Figure 16. Same as Figure 4, but for SBS 1116+583A.
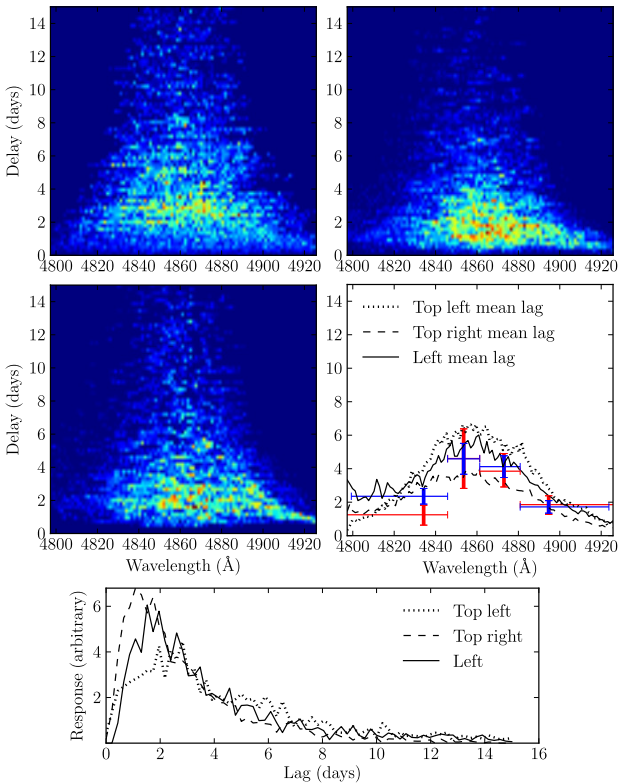
Figure 17. Same as Figure 5, but for SBS 1116+583A.

culated from cross-correlation time lags from Bentz et al. (2009) and line widths from Park et al. (2012a), we measure the f factors for SBS 1116+583A to be $\log_{10}(f_\sigma) = 0.96^{+0.32}_{-0.25}$ and $\log_{10}(f_{\rm FWHM}) = 0.34^{+0.32}_{-0.25}$ (see Section 4.1.1).

Three velocity-resolved transfer functions drawn randomly from the posterior and shown in Figure 17 show similar detailed structure. However, the strength of the prompt emission in the red wing varies between the velocity-resolved transfer functions, most prominent in the middle left panel of Figure 17 and least prominent in the top left panel. This is due to the variation in $f_{\rm ellip}$ and a preference for the remaining orbits to be inflowing. The velocity-integrated transfer functions also show consistent results, although the peakiness of the transfer function at lags of ~ 1 day varies.

4.2 Overview of Modeling Results

We will now give an overview of the similarities between the inferred BLR model parameters for the five objects in our sample. To begin with, the Hβ BLR geometry is consistent with a thick disk with preferential emission from the far side. While the minimum radius of the BLR from the central ionizing source and the dispersion or width of the BLR vary within our sample, the radial distribution shape is generally inferred to be exponential or between Gaussian and exponential.

For the dynamics, we generally infer either elliptical orbits, inflowing orbits, or a combination of the two. Both Arp 151 and NGC 5548 show clear signatures of inflow, while SBS 1116+583A shows clear signatures of elliptical orbits and NGC 6814 shows evidence for both inflow and elliptical orbits. In addition, both Arp 151 and NGC 5548 prefer bound inflowing orbits, a solution that is closer to the elliptical orbit solution. The absence of strong outflow dynamics in our sample is reassuring, since reverberation mapping relies on BLR gas dynamics being dominated by the gravitational potential of the black hole, although this is
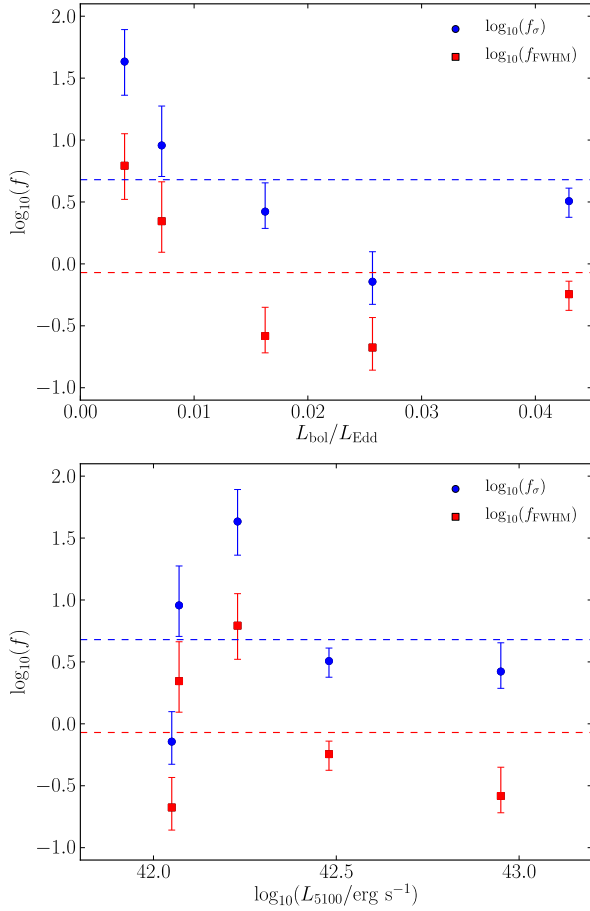
Figure 19. Individual f factors versus Eddington ratio (top panel) and AGN continuum luminosity, L_{5100} (bottom panel). The AGN luminosities at 5100Å are corrected for host galaxy contamination as described by Bentz et al. (2013) and the bolometric luminosities are calculated using a bolometric correction factor of nine. The blue circles show the values of $\log_{10}(f_\sigma)$, while the red squares show the values of $\log_{10}(f_{\mathrm{FWHM}})$. The values of $\langle\log_{10}(f_\sigma)\rangle$ and $\langle\log_{10}(f_{\mathrm{FWHM}})\rangle$ for the sample are shown by the top blue and bottom red dashed lines, respectively.

Figure 20. Individual f factors versus inclination angle as inferred by direct modeling. The values of $\langle\log_{10}(f_\sigma)\rangle$ and $\langle\log_{10}(f_{\mathrm{FWHM}})\rangle$ for the sample are shown by the blue dashed line in the top panel and the red dashed line in the bottom panel, respectively. Also shown as horizontal dotted, dot-dashed, and dashed lines are the mean f values by Park et al. (2012a), Woo et al. (2013), and Grier et al. (2013b) in the top panel, and values by Collin et al. (2006) and Yoon et al. (in preparation) in the bottom panel.

unsurprising given the low Eddington ratios of the objects in our sample.

We can also examine whether there are common degeneracies between the model parameters. The correlations between black hole mass, inclination angle, and opening angle are typically quite pronounced in our sample (see Figures 4, 7, 10, 13, and 16), and often the correlation between black hole mass and inclination angle is the strongest. This degeneracy is very important for BLRs viewed close to face-on, where the uncertainty in black hole mass becomes larger as the inclination angle approaches zero. Smaller opening angles accentuate the degeneracy, leading to strong correlations as for Mrk 1310 (see Figure 7). An interesting consequence of these degeneracies is what they predict for correlations of model parameters with individual values of the f factor.

As shown in Figure 18, there is no strong correlation between the f factor and black hole mass, as one might expect if the BLR geometry and dynamics are somehow corre-
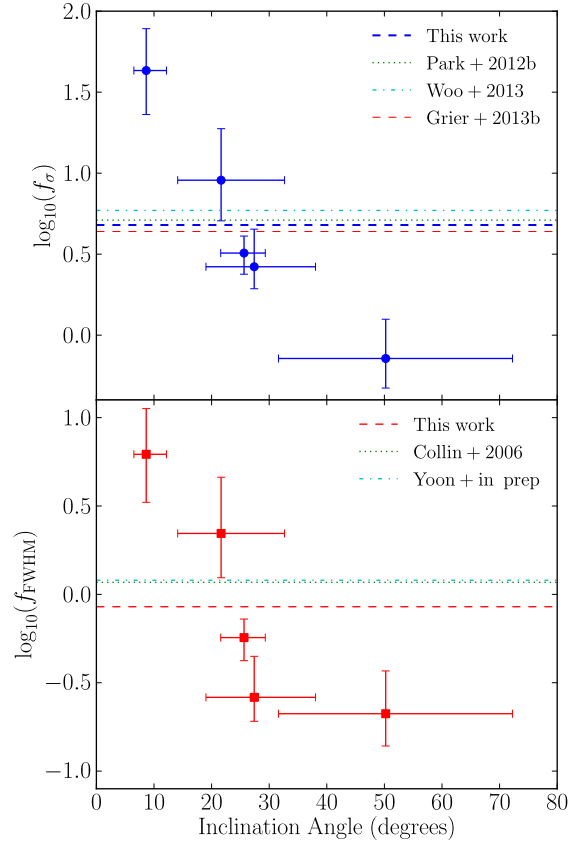
lated with the size of the black hole. There is also no strong correlation between the f factor and the Eddington ratio, $L_{\mathrm{bol}}/L_{\mathrm{Edd}}$, or the AGN continuum luminosity at 5100Å, L_{5100}, as shown in Figure 19. The AGN luminosities are corrected for host galaxy contamination by Bentz et al. (2013) and the Eddington ratios are calculated assuming a bolometric correction factor for $L(5100\text{Å})$ of nine. A correlation between f and the Eddington ratio might be expected if the BLR geometry or dynamics changed substantially with accretion rate, for example with contributions to the dynamics from radiation pressure. Since both f and the Eddington ratio are calculated using the values of M_{BH} inferred from dynamical modeling, the errors are correlated. For this reason we also plot f versus L_{5100}, as shown in the bottom panel of Figure 19, which does not have correlated errors, although it is not as closely related to accretion rate as the Eddington ratio since it has not been normalized by M_{BH}. However, there does appear to be a correlation between the f factor and inclination angle, as illustrated in Figure 20. Such a correlation was predicted by Goad et al. (2012) for a general class of BLR models similar to the ones used in our
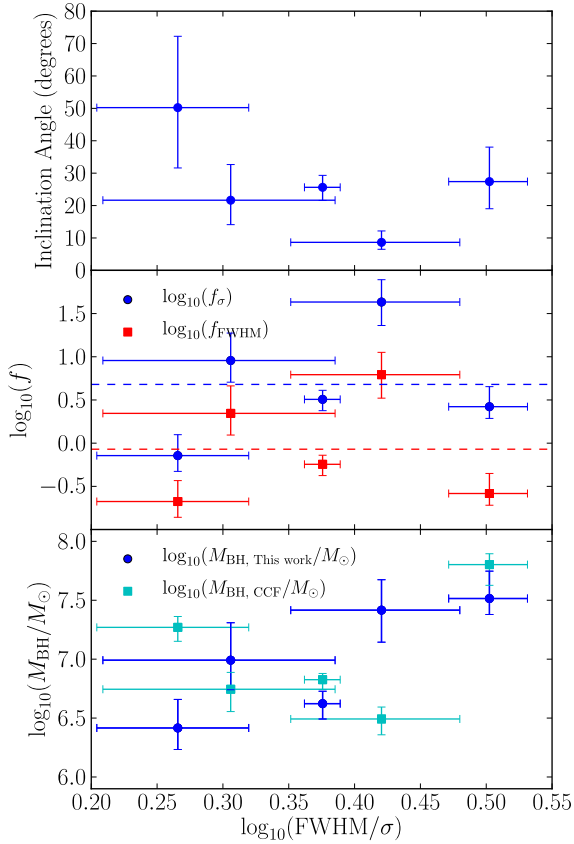
Figure 21. Inclination angle, f, and black hole mass as a function of the ratio of the FWHM to the line dispersion σ of the Hβ line. Line width measurements are from Park et al. (2012a). For a Gaussian distribution, $\log_{10}(\mathrm{FWHM}/\sigma) = 0.37$. In the middle panel, the values of $\langle\log_{10}(f_\sigma)\rangle$ and $\langle\log_{10}(f_{\mathrm{FWHM}})\rangle$ for the sample are shown by the top blue and bottom red dashed lines, respectively. In the bottom panel the black hole masses from cross-correlation function analysis and assuming $\log_{10}\langle f_\sigma\rangle = 0.71$ are plotted as light blue squares for comparison.

direct modeling analysis. Since the errors in black hole mass and f are the same, and since black hole mass correlates so strongly with inclination angle, one might expect to see at least a small trend between the f factor and inclination angle based only on correlated errors. Direct modeling on a larger sample of AGNs will allow us to quantify the contribution of correlated errors to the strength of the correlation between inclination angle and f.

On a related note, it has been suggested that the ratio of the FWHM to the line dispersion of broad emission lines is related to the inclination angle of the BLR to our line of sight (Collin et al. 2006; Goad et al. 2012). We use the FWHM and line dispersion measurements for the objects in our sample from Park et al. (2012a) to investigate the possibility of such trends, as shown in Figure 21. We find no strong correlation between $\log_{10}(\mathrm{FWHM}/\sigma)$ and the inclination angle or the f factors for individual AGNs, but we do find a tentative correlation between $\log_{10}(\mathrm{FWHM}/\sigma)$ and black hole mass. The trend of $\log_{10}(\mathrm{FWHM}/\sigma)$ with black hole mass is not seen for the virial product. A larger sample of AGNs with
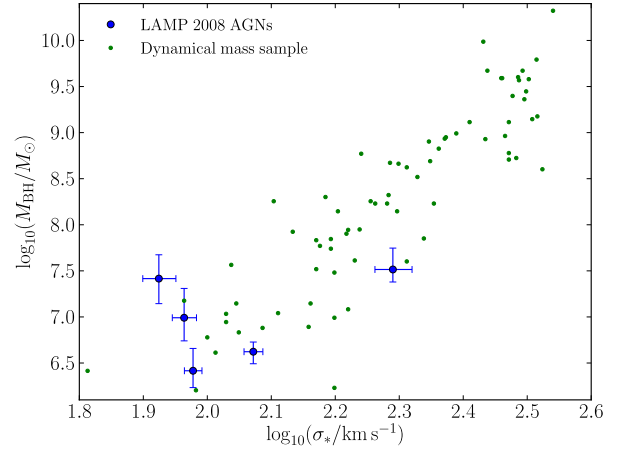

Figure 22. Black hole masses from our direct modeling approach and their host-galaxy stellar velocity dispersions, compared to the $M_{\mathrm{BH}}-\sigma_*$ relationship for black holes with masses from spatially-resolved stellar and gas dynamical modeling (as compiled by Woo et al. 2013). Measurements of the host-galaxy velocity dispersion for our sample of five LAMP 2008 objects are by Woo et al. (2010). Our sample is shown by the large blue circles with error bars. The dynamical mass sample is shown by the small green points.
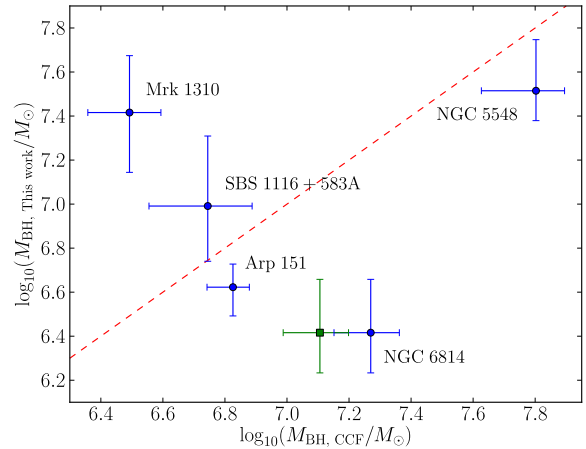

Figure 23. Comparison of the black hole mass estimates from our direct modeling approach on the y-axis versus the values measured using cross-correlation function analysis. The blue circles denote the sample using cross-correlation masses assuming $\log_{10}\langle f_\sigma\rangle = 0.71$, where the points corresponding to individual AGNs have been labeled. The single green square is for NGC 6814 for the case where the cross-correlation mass has been calculated using the time lag from our dynamical modeling instead of the time lag from cross-correlation. The red dashed line shows a slope of unity through the origin.

direct modeling analysis could clarify the strength of these correlations.

There are few independently measured quantities to compare with our direct modeling results. One of these is measurements of the time lag from cross-correlation function analysis, where we find good agreement within the uncertainties. Recently, Li et al. (2013) used our direct modeling formalism to develop an independent code to model

the geometry of the BLR. Their geometry model includes a Gamma distribution for the radial profile of gas, as well as an opening angle and inclination angle. In addition, their model includes non-linear response of the broad emission lines to changes in the continuum light curve. They measure the mean radius of the BLR for our sample of five AGNs using their geometry modeling code and obtain results that are mostly consistent with the results presented here. The one object for which our values of mean radius are inconsistent is NGC 6814, for which we measure a smaller value than both the mean lag by Bentz et al. (2009) of $\tau_{\rm cent} = 6.46^{+0.94}_{-0.96}$ days and the mean radius by Li et al. (2013) of $r_{\rm mean} = 6.9 \pm 0.7$ light days. The inconsistency between direct modeling results for NGC 6814 for the geometry model of Li et al. (2013) and the dynamical model implemented here could be caused by using the integrated line profiles versus the full spectral dataset, since for the full spectral dataset the model must fit not only the mean time lag but also the response as a function of velocity, placing more stringent constraints on the value of the mean radius. There are also a number of differences between the geometry model used here and the one used by Li et al. (2013), the most important being that we do not include non-linear response of the emission line flux, while Li et al. (2013) do not include asymmetry parameters such as κ, γ, or ξ in their model.

We can also compare our independent measurements of the black hole mass to those of quiescent and active galaxies with dynamical mass estimates. Using host galaxy velocity dispersion measurements by Woo et al. (2010), we overlay our five AGNs onto the dynamical mass sample from Woo et al. (2013) on the $M_{\rm BH} - \sigma_*$ relation, as shown in Figure 22. The five objects in our sample are consistent with the distribution of masses and stellar velocity dispersions in the dynamical sample, confirming that Seyfert 1 galaxies appear to lie on the same $M_{\rm BH} - \sigma_*$ as Seyfert 2 galaxies with black hole mass measurements from maser kinematics. With a larger sample of Seyfert 1 galaxies with direct modeling, we can test whether the agreement holds across the entire relation.

Another independently measured quantity is the mean f factor, $\langle f \rangle$, measured by aligning the $M_{\rm BH} - \sigma_*$ relations for quiescent and active galaxies. We will denote mean f factors that have been calculated using the dispersion of the RMS emission line profile by $\langle f_\sigma \rangle$ and those that have been calculated using the FWHM of the mean emission line profile by $\langle f_{\rm FWHM} \rangle$. Values of $\langle f_\sigma \rangle$ from the literature include $\log_{10}\langle f_\sigma \rangle = 0.74^{+0.12}_{-0.17}$ (Onken et al. 2004), $\log_{10}\langle f_\sigma \rangle = 0.72^{+0.09}_{-0.10}$ (Woo et al. 2010), $\log_{10}\langle f_\sigma \rangle = 0.45 \pm 0.09$ (Graham et al. 2011), $\log_{10}\langle f_\sigma \rangle = 0.71 \pm 0.11$ (Park et al. 2012b), $\log_{10}\langle f_\sigma \rangle = 0.77 \pm 0.13$ (Woo et al. 2013), and $\log_{10}\langle f_\sigma \rangle = 0.64^{+0.10}_{-0.12}$ (Grier et al. 2013b). These values agree to within the uncertainties except for the value by Graham et al. (2011), for which the discrepancy is explained by sample selection and choice of the independent variable when fitting for f. We choose to adopt the Park et al. (2012b) value of $\log_{10}\langle f_\sigma \rangle = 0.71$ for calculations of the black hole mass using the virial product, since it is midway between the two most recent values of $\log_{10}\langle f_\sigma \rangle$ by Woo et al. (2013) and Grier et al. (2013b) and the difference between either measurement and the Park et al. (2012b) value is within the quoted error bars.

The f_σ factors measured individually for the five ob-

jects in our sample and listed in Table 3 are generally consistent to within the uncertainties with all of these values, although the low value of f_σ for NGC 6814 is only marginally consistent with the higher $\langle f_\sigma \rangle$ values (Onken et al. 2004; Woo et al. 2010; Park et al. 2012b; Woo et al. 2013; Grier et al. 2013b). Part of the discrepancy for NGC 6814 may be due to the difference in time lags between the value measured from the cross-correlation function of $\tau_{\rm cent} = 6.46^{+0.94}_{-0.96}$ days (Bentz et al. 2009) and the value we infer from direct modeling of $\tau_{\rm mean} = 4.43^{+0.72}_{-0.83}$ days. Using our measurement of the time lag to calculate the virial mass increases the value of f_σ by 0.16 dex to $\log_{10}(f_\sigma) = 0.02^{+0.24}_{-0.18}$ for NGC 6814. To better illustrate this issue, a comparison of our independent measurements of black hole mass to those measured using cross-correlation function analysis and assuming $\log_{10}\langle f_\sigma \rangle = 0.71$ (Park et al. 2012b) is shown in Figure 23. NGC 6814 has one of the most discrepant measurements of the black hole mass, and the discrepancy is reduced when the cross-correlation mass is calculated using the smaller time lag we infer from direct modeling. However, since the posterior PDF for the black hole mass in NGC 6814 extends up to values of $\log_{10}(M_{\rm BH}/M_\odot) \sim 7.3$, this means the posterior PDF for f_σ also extends up to values consistent with the higher $\langle f_\sigma \rangle$ values. While the high posterior median value of f_σ for Mrk 1310 is also only marginally consistent with the higher $\langle f_\sigma \rangle$ values, the posterior PDF for black hole mass for Mrk 1310 extends down to values below $\log_{10}(M_{\rm BH}/M_\odot) \sim 6.5$ and hence the posterior PDF for f_σ also extends down to values consistent with the higher $\langle f_\sigma \rangle$ values.

There are fewer measurements of $f_{\rm FWHM}$ in the literature. Collin et al. (2006) find $\log_{10}\langle f_{\rm FWHM} \rangle = 0.07^{+0.15}_{-0.24}$, in good agreement with the more recently calculated value of $\log_{10}\langle f_{\rm FWHM} \rangle = 0.08 \pm 0.12$ from Yoon et al. (in preparation). While three of the AGNs in our sample have values of $f_{\rm FWHM}$ consistent with the mean value of Yoon et al., Mrk 1310 and NGC 6814 have values that are only marginally consistent.

4.3   The Mean f factor for LAMP 2008

With five independent black hole mass measurements we can now calculate the mean f factors for our AGN sample, called $\langle f_\sigma \rangle$ and $\langle f_{\rm FWHM} \rangle$. We use the full posterior distributions of f for each AGN to measure the mean and the dispersion of the distribution of f factors for the whole sample, as described in Appendix B. We measure a value for $\langle \log_{10}(f_\sigma) \rangle$ of 0.68 ± 0.40 and a dispersion for $\log_{10}(f_\sigma)$ of 0.75 ± 0.40, while we measure a value for $\langle \log_{10} f_{\rm FWHM} \rangle$ of -0.07 ± 0.40 and a dispersion for $\log_{10}(f_{\rm FWHM})$ of 0.77 ± 0.38. The posterior distributions for $\langle \log_{10}(f_\sigma) \rangle$ and $\langle \log_{10}(f_{\rm FWHM}) \rangle$ and the predictive distributions for new measurements of $\log_{10}(f_\sigma)$ and $\log_{10}(f_{\rm FWHM})$ are illustrated in Figure 24. The predictive distribution is the distribution from which new measurements of f are drawn and is wider than the posterior for the mean value due to the large scatter in individual f posterior distributions. Both our values of $\langle f_\sigma \rangle$ and its dispersion are consistent to within the uncertainties with the values for $\langle f_\sigma \rangle$ measured by aligning the $M_{\rm BH} - \sigma_*$ relation for active galaxies with the relation for galaxies with dynamical mass estimates (e.g. Onken et al. 2004; Woo et al. 2010; Graham et al. 2011; Park et al. 2012b; Woo et al. 2013; Grier
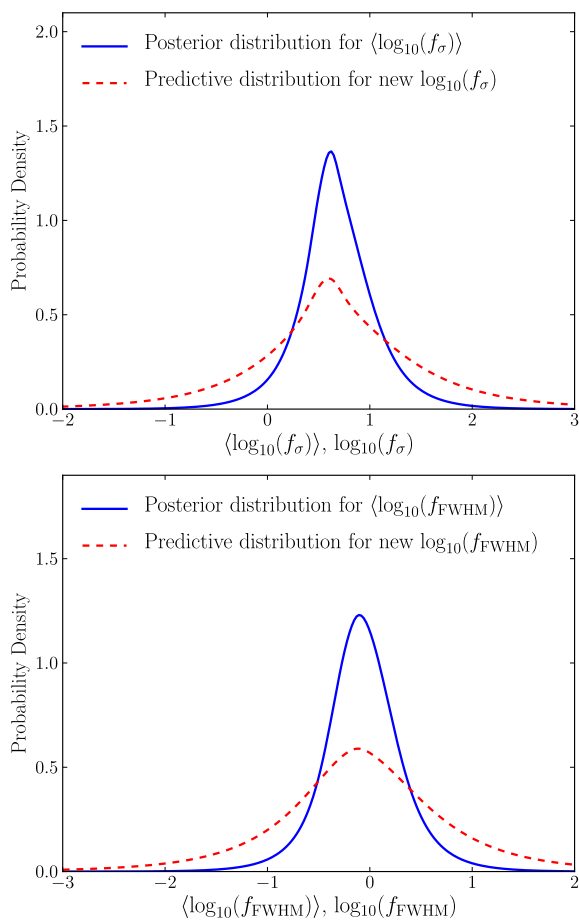
Figure 24. Top: The posterior distribution for $\langle \log_{10}(f_\sigma) \rangle$, the mean of the f_σ factor distribution for our sample of five AGNs, is shown by the solid blue line. The predictive distribution for new measurements of $\log_{10}(f_\sigma)$ is shown by the dashed red line. Bottom: The posterior distribution for $\langle \log_{10}(f_{\rm FWHM}) \rangle$, the mean of the $f_{\rm FWHM}$ factor distribution for our sample of five AGNs, is shown by the solid blue line. The predictive distribution for new measurements of $\log_{10}(f_{\rm FWHM})$ is shown by the dashed red line.

et al. 2013b). Similarly, our values of $\langle f_{\rm FWHM} \rangle$ and its dispersion are consistent to within the uncertainties with the values measured by Collin et al. (2006) and Yoon et al. (in preparation). The mean f factors derived here are meant to illustrate the capabilities of the direct modeling approach and should not be used to normalize the black hole masses of reverberation mapped AGNs until the direct modeling sample is both larger and more representative of the overall AGN population.

5   CONCLUSIONS

We have applied direct modeling techniques to a sample of five AGNs from the LAMP 2008 reverberation mapping campaign in order to constrain the geometry and dynamics of the Hβ BLR. Direct modeling also allows us to measure the black hole mass independently and, by comparison with the virial product from traditional reverberation mapping analysis, to measure the virial coefficient or f factor for in-

dividual AGNs. We have also measured the mean f factor for our sample, a number that determines the absolute mass scaling for the whole reverberation mapping sample. Our main results are as follows:

(i) The geometry of the BLR is consistent with a thick disk. The radial distribution of Hβ emitting gas is closer to exponential than Gaussian and is viewed closer to face-on than edge-on. For Arp 151 we find a more detailed geometry of a half-cone, where the Hβ emission is concentrated towards the outer faces of the disk and the disk mid-plane is mostly opaque, similar to the bowl BLR geometry proposed by Goad et al. (2012).

(ii) There is preferential Hβ emission from the far side of the BLR with respect to the observer, consistent with models where the BLR gas is self-shielding.

(iii) The dynamics of the BLR are consistent with in-flowing motions, elliptical orbits, or a combination of both. Specifically, the dynamics of Arp 151 are inferred to be in-flowing motions, in agreement with velocity-resolved cross-correlation lag measurements (Bentz et al. 2009) and reconstruction of the transfer function using maximum entropy techniques (Bentz et al. 2010).

(iv) The black hole masses for the five objects in our sample are $\log_{10}(M_{\rm BH}/M_\odot) = 6.62^{+0.10}_{-0.13}$ for Arp 151, $7.42^{+0.26}_{-0.27}$ for Mrk 1310, $7.51^{+0.23}_{-0.14}$ for NGC 5548, $6.42^{+0.24}_{-0.18}$ for NGC 6814, and $6.99^{+0.32}_{-0.25}$ for SBS 1116+583A.

(v) Using our measurements of the black hole mass and virial products based on the dispersion of the RMS line profile, we measure the f factors for the AGNs in our sample to be $\log_{10}(f_\sigma) = 0.51^{+0.10}_{-0.13}$ for Arp 151, $1.63^{+0.26}_{-0.27}$ for Mrk 1310, $0.42^{+0.23}_{-0.14}$ for NGC 5548, $-0.14^{+0.24}_{-0.18}$ for NGC 6814, and $0.96^{+0.32}_{-0.25}$ for SBS 1116+583A. Using instead the virial products based on the FWHM of the mean line profile, we find that $\log_{10}(f_{\rm FWHM}) = -0.24^{+0.10}_{-0.13}$ for Arp 151, $0.79^{+0.26}_{-0.27}$ for Mrk 1310, $-0.58^{+0.23}_{-0.14}$ for NGC 5548, $-0.68^{+0.24}_{-0.18}$ for NGC 6814, and $0.34^{+0.32}_{-0.25}$ for SBS 1116+583A.

(vi) The f factors for individual AGNs are correlated with inclination angle, but not with black hole mass, AGN optical luminosity, or Eddington ratio.

(vii) Neither the f factors nor the inclination angles for individual AGNs are strongly correlated with the ratio of the FWHM to the line dispersion in the mean Hβ spectrum, as would be expected if line shape correlated strongly with viewing angle of the BLR. However, we do find a tentative correlation between the ratio of the FWHM to the line dispersion and black hole mass.

(viii) By combining the posterior distributions of f for each AGN, we measure mean values of f for the sample. With virial products based on the dispersion of the RMS line profile, we measure a mean value of $\log_{10}(f_\sigma)$ of 0.68 ± 0.40 with a dispersion in $\log_{10}(f_\sigma)$ of 0.75 ± 0.40, and using virial products based on the FWHM of the mean line profile we measure a mean $\log_{10}(f_{\rm FWHM})$ value of -0.07 ± 0.40 with a dispersion in $\log_{10}(f_{\rm FWHM})$ of 0.77 ± 0.38. These values of the mean f factor are meant to illustrate the capabilities of the direct modeling approach and should not be used to calibrate black hole masses from reverberation mapping until the sample size is larger and more representative of the overall AGN population.

The modeling results presented here demonstrate the capabilities of the direct modeling approach and show that

Table 2. Inferred posterior median parameter values and central 68% credible intervals for direct modeling of five LAMP 2008 AGNs.

Geometry Model Parameter	Arp 151	Mrk 1310	NGC 5548	NGC 6814	SBS 1116+583A
r_{mean} (light days)	$3.44^{+0.26}_{-0.24}$	$3.13^{+0.42}_{-0.40}$	$3.31^{+0.66}_{-0.61}$	$3.76^{+1.15}_{-0.77}$	$4.07^{+0.79}_{-0.65}$
r_{min} (light days)	$0.44^{+0.13}_{-0.20}$	$0.12^{+0.19}_{-0.08}$	$1.39^{+0.80}_{-1.01}$	$0.15^{+0.19}_{-0.11}$	$0.93^{+0.50}_{-0.49}$
σ_r (light days)	$3.72^{+0.45}_{-0.43}$	$2.59^{+0.42}_{-0.35}$	$1.50^{+0.73}_{-0.60}$	$3.75^{+1.05}_{-0.69}$	$3.14^{+0.81}_{-0.66}$
τ_{mean} (days)	$3.07^{+0.25}_{-0.20}$	$2.96^{+0.42}_{-0.35}$	$3.22^{+0.66}_{-0.54}$	$4.43^{+0.72}_{-0.83}$	$3.78^{+0.57}_{-0.52}$
τ_{median} (days)	$1.75^{+0.28}_{-0.23}$	$2.26^{+0.35}_{-0.31}$	$2.77^{+0.63}_{-0.42}$	$2.67^{+0.60}_{-0.61}$	$2.71^{+0.40}_{-0.37}$
β	$1.25^{+0.15}_{-0.16}$	$0.89^{+0.10}_{-0.10}$	$0.80^{+0.60}_{-0.31}$	$1.07^{+0.08}_{-0.09}$	$1.00^{+0.27}_{-0.21}$
θ_o (degrees)	$25.6^{+3.7}_{-4.0}$	$8.6^{+3.5}_{-2.1}$	$27.4^{+10.6}_{-8.4}$	$50.2^{+22.0}_{-18.6}$	$21.7^{+11.0}_{-7.5}$
θ_i (degrees)	$25.2^{+3.3}_{-3.4}$	$6.6^{+5.0}_{-2.5}$	$38.8^{+12.1}_{-11.4}$	$49.4^{+20.4}_{-22.2}$	$18.2^{+8.4}_{-5.9}$
κ	$-0.36^{+0.08}_{-0.08}$	$-0.04^{+0.38}_{-0.35}$	$-0.24^{+0.06}_{-0.13}$	$-0.44^{+0.10}_{-0.05}$	$-0.03^{+0.31}_{-0.34}$
γ	$4.27^{+0.54}_{-0.80}$	$2.97^{+1.38}_{-1.43}$	$2.01^{+1.78}_{-0.71}$	$2.91^{+1.37}_{-1.31}$	$3.19^{+1.21}_{-1.37}$
ξ	$0.09^{+0.08}_{-0.05}$	$0.40^{+0.38}_{-0.29}$	$0.34^{+0.11}_{-0.18}$	$0.71^{+0.22}_{-0.33}$	$0.61^{+0.28}_{-0.37}$
Dynamical Model Parameter	**Arp 151**	**Mrk 1310**	**NGC 5548**	**NGC 6814**	**SBS 1116+583A**
$\log_{10}(M_{\mathrm{BH}}/M_\odot)$	$6.62^{+0.10}_{-0.13}$	$7.42^{+0.26}_{-0.27}$	$7.51^{+0.23}_{-0.14}$	$6.42^{+0.24}_{-0.18}$	$6.99^{+0.32}_{-0.25}$
f_{ellip}	$0.06^{+0.09}_{-0.05}$	$0.56^{+0.34}_{-0.39}$	$0.23^{+0.15}_{-0.15}$	$0.32^{+0.17}_{-0.22}$	$0.66^{+0.21}_{-0.27}$
f_{flow}	$0.24^{+0.20}_{-0.17}$	$0.65^{+0.24}_{-0.38}$	$0.25^{+0.21}_{-0.16}$	$0.29^{+0.25}_{-0.19}$	$0.31^{+0.31}_{-0.22}$
θ_e (degrees)	$12.0^{+10.7}_{-8.3}$	$57.2^{+24.9}_{-41.0}$	$21.3^{+21.4}_{-14.7}$	$47.0^{+16.7}_{-26.5}$	$49.7^{+28.8}_{-32.1}$
σ_{turb}	$0.008^{+0.028}_{-0.007}$	$0.004^{+0.010}_{-0.003}$	$0.016^{+0.044}_{-0.013}$	$0.013^{+0.036}_{-0.011}$	$0.011^{+0.033}_{-0.009}$

The definitions of the geometry and dynamical model parameters can be found in Appendix A.

Table 3. Inferred posterior median parameter values and central 68% credible intervals for f factors of five LAMP 2008 AGNs. The f factor corresponding to the difference between black hole mass and the virial product measured using the dispersion of the RMS line profile is given as f_σ, while the one corresponding to a virial product measured using the FWHM of the mean line profile is given as f_{FWHM}.

Object	$\log_{10}(f_\sigma)$	$\log_{10}(f_{\mathrm{FWHM}})$
Arp 151	$0.51^{+0.10}_{-0.13}$	$-0.24^{+0.10}_{-0.13}$
Mrk 1310	$1.63^{+0.26}_{-0.27}$	$0.79^{+0.26}_{-0.27}$
NGC 5548	$0.42^{+0.23}_{-0.14}$	$-0.58^{+0.23}_{-0.14}$
NGC 6814	$-0.14^{+0.24}_{-0.18}$	$-0.68^{+0.24}_{-0.18}$
SBS 1116+583A	$0.96^{+0.32}_{-0.25}$	$0.34^{+0.32}_{-0.25}$

significant information about the BLR geometry and dynamics is encoded in high-quality reverberation mapping datasets. We find that the five AGNs in our sample have similar geometric and kinematic features, suggesting that the BLR may also be similar in other Seyfert 1 galaxies with low luminosities, black hole masses of $10^{6.5-7.5} M_\odot$, and small Eddington ratios. By applying the direct modeling approach to a larger sample of AGNs, we can determine if and how the properties of the BLR might change with increasing luminosity, accretion rate, and black hole mass.

Our results also demonstrate the feasibility of measuring black hole masses independently of the f factor in Seyfert 1 galaxies. For the reverberation mapping datasets shown here, black hole masses can be constrained to $0.15 - 0.3$ dex uncertainty depending upon data quality and degeneracy of the black hole mass with the geometrical properties of the BLR, such as inclination angle of the observer and opening angle of the disk. In addition, the BLR kinematics inferred for our sample are consistent with bound orbits, suggesting that the Hβ-emitting BLR is not significantly affected by disk winds or outflows. This is an important consistency check for reverberation mapped black hole masses because they are measured by assuming the BLR gas orbits are dominated by the gravity of the black hole. Future versions of our BLR model will explore the issue of non-gravitational forces further and relate broad line emission to the properties of the emitting gas by incorporating the results of photoionization physics.

REFERENCES

Antonucci, R. 1993, ARA&A, 31, 473

Barth, A. J., Nguyen, M. L., Malkan, M. A., et al. 2011, ApJ, 732, 121

Barth, A. J., Pancoast, A., Thorman, S. J., et al. 2011b, ApJ, 743, L4

Bentz, M. C., Peterson, B. M., Pogge, R. W., Vestergaard, M., & Onken, C. A. 2006, ApJ, 644, 133

Bentz, M. C., et al. 2009, ApJ, 705, 199

Bentz, M. C., et al. 2010, ApJ, 720, L46

Bentz, M. C., Denney, K. D., Grier, C. J., et al. 2013, ApJ, 767, 149

Blandford, R. D., & McKee, C. F. 1982, ApJ, 255, 419

Brewer B. J., Pártay L. B., Csányi G., 2011b, Statistics and Computing, 21, 4, 649-656. arXiv:0912.2380

Brewer, B. J., et al. 2011a, ApJ, 733, L33

Brewer B. J., Elliott T. M., 2014, MNRAS, 439, L31

Collin, S., Kawaguchi, T., Peterson, B. M., & Vestergaard, M. 2006, A&A, 456, 75

Denney, K. D., et al. 2010, ApJ, 721, 715

Goad, M. R., Korista, K. T., & Ruff, A. J. 2012, MNRAS, 426, 3086

Graham, A. W., Onken, C. A., Athanassoula, E., & Combes, F. 2011, MNRAS, 412, 2211

Greene, J. E., Peng, C. Y., Kim, M., et al. 2010b, ApJ, 721, 26

Grier, C. J., Peterson, B. M., Horne, K., et al. 2013a, ApJ, 764, 47

Grier, C. J., Martini, P., Watson, L. C., et al. 2013b, ApJ, 773, 90

Hogg D. W., Myers A. D., Bovy J., 2010, ApJ, 725, 2166

Horne, K., Welsh, W. F., & Peterson, B. M. 1991, ApJL, 367, L5

Horne, K. 1994, in ASP Conf. Ser. 69, Reverberation Mapping of the Broad-line Region in Active Galactic Nuclei, ed. P. M. Gondhalekar, K. Horne, & B. M. Peterson (San Francisco, CA: ASP), 23

Kaspi, S., Smith, P. S., Netzer, H., Maoz, D., Jannuzi, B. T., & Giveon, U. 2000, ApJ, 533, 631

Kelly, B. C., Bechtold, J., & Siemiginowska, A. 2009, ApJ, 698, 895

Kozłowski, S., Kochanek, C. S., Udalski, A., et al. 2010, ApJ, 708, 927

Krolik, J. H., & Done, C. 1995, ApJ, 440, 166

Li, Y.-R., Wang, J.-M., Ho, L. C., Du, P., & Bai, J.-M. 2013, arXiv:1310.3907

MacLeod, C. L., Ivezić, Ž., Kochanek, C. S., et al. 2010, ApJ, 721, 1014

McGill, K. L., Woo, J.-H., Treu, T., & Malkan, M. A. 2008, ApJ, 673, 703

Onken, C. A., Ferrarese, L., Merritt, D., Peterson, B. M., Pogge, R. W., Vestergaard, M., & Wandel, A. 2004, ApJ, 615, 645

Pancoast, A., Brewer, B. J., & Treu, T. 2011, ApJ, 730, 139

Pancoast, A., Brewer, B. J., Treu, T., et al. 2012, ApJ

Pancoast, A., Brewer, B. J., & Treu, T. 2014, Submitted to MNRAS, Available on ArXiv e-prints.

Park, D., Woo, J.-H., Treu, T., et al. 2012a, ApJ, 747, 30

Park, D., Kelly, B. C., Woo, J.-H., & Treu, T. 2012b, ApJS, 203, 6

Peterson, B. M. 1993, PASP, 105, 247

Peterson, B. M., et al. 2004, ApJ, 613, 682

Urry, C. M., & Padovani, P. 1995, PASP, 107, 803

Vestergaard, M., & Peterson, B. M. 2006, ApJ, 641, 689

Vestergaard, M. 2011, in Black Holes, Space Telescope Science Institute Symposium Series vol. 21, edited by M. Livio & A. M. Koekemoer (Cambridge University Press), 150

Walsh, J. L., et al. 2009, ApJS, 185, 156

Wandel, A., Peterson, B. M., & Malkan, M. A. 1999, ApJ, 526, 579

Whittle, M. 1992, ApJS, 79, 49

Woo, J.-H., Treu, T., Barth, A. J., et al. 2010, ApJ, 716, 269

Woo, J.-H., Schulze, A., Park, D., et al. 2013, ApJ, 772, 49

Zu, Y., Kochanek, C. S., & Peterson, B. M. 2011, ApJ, 735, 80

Zu, Y., Kochanek, C. S., Kozłowski, S., & Udalski, A. 2012, arXiv:1202.3783

APPENDIX A: DEFINITION OF MODEL PARAMETERS

A1   Geometry Model Parameters

We use a Gamma distribution to model the radial distribution of point particles in the BLR:

$$p(x|\alpha, \theta) \propto x^{\alpha-1} \exp\left(-\frac{x}{\theta}\right). \tag{A1}$$

We then allow the Gamma distribution to be offset from the origin by an amount $r_{\min}$ plus the Schwarzschild radius, $R_s = 2GM/c^2$, and perform a change of variables between (α, θ) and (μ, β, F) such that

$$\mu = R_s + r_{\min} + \alpha\theta \tag{A2}$$

$$\beta = \frac{1}{\sqrt{\alpha}} \tag{A3}$$

$$F = \frac{r_{\min}}{r_{\min} + \alpha\theta} \tag{A4}$$

where μ is the mean radius, β determines the shape of the Gamma distribution, and F is the fraction of μ corresponding to $r_{\min}$. The prior on μ is uniform in the log of the parameter between 1.02×10^{-3} light days and the time span between the first and last measurement of the continuum or line flux, while the prior on β is uniform between 0 and 2 and the prior on F is uniform between 0 and 1. The standard deviation for the radial distribution is given by $\sigma_r = \mu\beta(1 - F)$. We can also calculate the numerical mean radius r_{mean}, the numerical mean time lag τ_{mean}, and the numerical median time lag τ_{median} for a specific realization of point particle positions. The direct modeling results in Table 2 include values for r_{mean}, $r_{\min}$, σ_r, τ, and β. The geometry of the BLR is further defined by θ_o, the half-opening angle of the BLR disk. Values of $\theta_o \to 0$ (90) degrees correspond to thin disk (spherical) geometries and the prior is uniform between 0 and 90 degrees. The inclination angle, θ_i, is the angle by which an observer views the BLR. Values of $\theta_i \to 0$ (90) degrees correspond to face-on (edge-on) geometries and the prior is uniform in the cosine of the inclination angle between 0 and 90 degrees. We weight the emission from each point particle by a cosine function:

$$W(\phi) = \frac{1}{2} + \kappa \cos \phi. \tag{A5}$$

where W is the weight (between 0 and 1) given to each point particle, ϕ is the angle between the observer's line of sight to the central source and the point particle's line of sight to the central source, and κ is a parameter with uniform prior between -0.5 and 0.5. Values of $\kappa \to -0.5$ (0.5) correspond to the far (near) side of the BLR producing more line emission. We also include the option for preferential emission from the faces of the BLR disk by changing the angle θ for a point particle's displacement from a flat to thick disk, given by

$$\theta = \mathrm{acos}\left(\cos \theta_o + (1 - \cos \theta_o) \times U^\gamma\right) \tag{A6}$$

where U is a random number drawn uniformly between the values of 0 and 1. Values of $\gamma \to 1$ (5) correspond to uniform concentrations of point particles in the disk (more point particles along the faces of the disk), where γ has a uniform prior between 1 and 5. Finally, we allow the midplane of the BLR to range between opaque and transparent, where ξ is the fraction of the point particles below the midplane that are not moved to the top half. For $\xi \to 1$ (0) the midplane is transparent (opaque), where ξ has a uniform prior between 0 and 1.

A2   Dynamical Model Parameters

The dynamics of the BLR are determined by the black hole mass, M_{BH}, which has a uniform prior in the log of the parameter between 2.78×10^4 and $1.67 \times 10^9 M_\odot$. We draw the velocities for the point particles from two distributions in the plane of radial and tangential velocities. The fraction of point particles with velocities drawn from the distribution centered around the circular orbit value is given by f_{ellip}, which has a uniform prior between 0 and 1. The remaining point particles have velocities drawn from the distribution centered around either the radial inflowing or outflowing escape velocity values, where $0 < f_{\mathrm{flow}} < 0.5$ corresponds to the inflowing distribution and $0.5 < f_{\mathrm{flow}} < 1$ corresponds to the outflowing distribution, and where f_{flow} has a uniform prior between 0 and 1. The inflow/outflow-centered distributions can also be rotated by an angle θ_e towards the circular orbit-centered distribution, where θ_e has a uniform prior between 0 and 90 degrees. Finally, we include additional macroturbulent velocities given by:

$$v_{\mathrm{turb}} = \mathcal{N}(0, \sigma_{\mathrm{turb}})|v_{\mathrm{circ}}| \tag{A7}$$

where v_{circ} is the circular orbit velocity and σ_{turb} is the standard deviation of the Gaussian distribution from which a random macroturbulent velocity component is drawn. σ_{turb} has a uniform prior in the log of the parameter between 0.001 and 0.1.

APPENDIX B: CALCULATING THE MEAN f FACTOR

For each of the five AGNs in our sample, we can compute the posterior distribution for the f factor that relates the black hole mass to either the velocity dispersion or the FWHM of the broad emission line. Here we describe the method used to

constrain the distribution of f values from the modelling results (see Hogg, Myers & Bovy 2010; Brewer & Elliott 2014, for examples using the same approach). Consider a collection of N objects, each of which has a property θ which we infer from data D. Modelling each object yields a posterior distribution

$$p(\theta_i|D_i) \propto \pi(\theta_i)p(D_i|\theta_i) \tag{B1}$$

where $\pi(\theta_i)$ is the prior used in the modelling, which is the same for each object. In practice, since we are using MCMC, the posterior distributions $p(\theta_i|D_i)$ are represented computationally by samples. In our particular application, $\theta \equiv \log_{10}(f)$.

Unfortunately, the use of the $\pi(\theta_i)$ prior for each object implies we do not expect the objects to be clustered around a typical θ value. If we did expect such clustering, we should have used a different prior for the $\{\theta_i\}$, such as a normal distribution:

$$p(\{\theta_i\}|\mu_\theta, \sigma_\theta) \quad = \quad \prod_{i=1}^{N} \frac{1}{\sigma_\theta\sqrt{2\pi}} \exp\left[-\frac{1}{2\sigma_\theta^2}\left(\theta_i - \mu_\theta\right)^2\right] \tag{B2}$$

This is the prior, conditional on two new hyperparameters describing the typical value μ_θ that the objects are clustered around, and the scatter σ_θ. To complete the inference we also need to assign a prior to μ_θ and σ_θ, which we take to be vague. Using this model, we can summarise our uncertainty about the properties of the sample by calculating the posterior distribution for μ_θ and σ_θ. Alternatively the posterior distribution for the *actual* mean $\frac{1}{N}\sum_{i=1}^{N}\theta_i$ could be calculated, but the former approach allows for generalisation beyond the current sample.

The posterior distribution for the hyperparameters is

$$p(\mu_\theta, \sigma_\theta|\{D_i\}) \quad \propto \quad p(\mu_\theta, \sigma_\theta)p(\{D_i\}|\mu_\theta, \sigma_\theta) \tag{B3}$$

$$\propto \quad p(\mu_\theta, \sigma_\theta)\int \prod_{i=1}^{N} p(\theta_i, D_i|\mu_\theta, \sigma_\theta)\, d^N\theta_i \tag{B4}$$

$$\propto \quad p(\mu_\theta, \sigma_\theta)\int \prod_{i=1}^{N} p(\theta_i|\mu_\theta, \sigma_\theta)p(D_i|\theta_i, \mu_\theta, \sigma_\theta)\, d^N\theta_i \tag{B5}$$

$$\propto \quad p(\mu_\theta, \sigma_\theta)\int \prod_{i=1}^{N} p(\theta_i|\mu_\theta, \sigma_\theta)p(D_i|\theta_i)\, d^N\theta_i \tag{B6}$$

$$\propto \quad p(\mu_\theta, \sigma_\theta)\int \prod_{i=1}^{N} p(\theta_i|\mu_\theta, \sigma_\theta)\frac{\pi(\theta_i)}{\pi(\theta_i)}p(D_i|\theta_i)\, d^N\theta_i \tag{B7}$$

$$\propto \quad p(\mu_\theta, \sigma_\theta)\prod_{i=1}^{N}\left\langle \frac{p(\theta_i|\mu_\theta, \sigma_\theta)}{\pi(\theta_i)}\right\rangle. \tag{B8}$$

where the expectation is taken with respect to the posterior distributions we have actually sampled, and can be computed straightforwardly. Essentially, Eq B8 favors $(\mu_\theta, \sigma_\theta)$ values that place a lot of probability in regions that overlap with the posteriors that we found.